Available online at www.sciencedirect.com

SCIENCE DIRECT®

Earth and Planetary Science Letters 228 (2004) 525–546

EPSL

www.elsevier.com/locate/epsl

Distinct mantle sources of low-Ti and high-Ti basalts from the western Emeishan large igneous province, SW China: implications for plume–lithosphere interaction

Long Xiao[a,b,*], Y.G. Xu[a], H.J. Mei[a], Y.F. Zheng[c], B. He[a], Franco Pirajno[d]

[a]*Guangzhou Institute of Geochemistry, Chinese Academy of Sciences, Guangzhou 510640, PR China*
[b]*Faculty of Earth Sciences, China University of Geosciences, Wuhan 430074, PR China*
[c]*School of Earth and Space Sciences, University of Science and Technology of China, Hefei 230026, PR China*
[d]*Geological Survey of Western Australia, 100 Plain Street, East Perth WA 6004, Australia*

Received 15 December 2003; received in revised form 16 September 2004; accepted 1 October 2004
Available online 5 November 2004
Editor: V. Courtillot

Abstract

The Late Permian Emeishan large igneous province (ELIP), with an areal extent of over 500,000 km^2, at the western margin of Yangtze craton, is increasingly regarded as the result of the impingement of a mantle plume onto the lithosphere. However, petrogenesis of the continental flood basalt remains controversial. The best-exposed lava succession in the western ELIP is studied in order to further constrain their petrogenesis and plume–lithosphere interaction. The basaltic lava flows of the ELIP are geochemically classified into low-Ti (LT) and high-Ti (HT) types. The LT type lavas exhibit low Ti/Y (<500) and εNd(t) (−0.34~−3.76) but comparatively high Mg# (44–67) and (^{87}Sr/^{86}Sr)$_i$ (0.705–0.708), whereas the HT type lavas have high Ti/Y (>500), εNd(t) (−1.17~0.43) but lower Mg# (31–53) and (^{87}Sr/^{86}Sr)$_i$ (0.705–0706). The LT basalts can be further subdivided into: LT1 and LT2. LT1 lavas exhibit relatively higher Mg# (51–67) and (^{87}Sr/^{86}Sr)$_i$ ratio (0.706–0.707), lower Nb/La ratio (<0.9) and initial εNd(t) (−6.74~−0.34) than the LT2 type lavas (Nb/La>1.1; εNd(t)=−1.17~0.43). Detailed stratigraphic work indicates that there was a temporal progression from LT1 to LT2 to HT-type magmas. This compositional shift cannot be explained simply in terms of a declining extent of crustal contamination of a mantle-derived melt with time. Instead, it seems that the LT and HT type magmas originated from distinct mantle sources and parental magmas. Geochemical features of the early stage LT1 lavas are indicative of a significant contribution from the enriched continental lithosphere mantle, whereas the compositional shift from LT1 to LT2 reveals a trend from predominantly shallower lithospheric mantle to deeper mantle with time. Late stage HT magma formed from a deeper mantle source that may possibly be a mantle plume.

Keywords: Emeishan; SW China; high-Ti and low-Ti basalts; petrogenesis; mantle plume; lithosphere

* Corresponding author. Faculty of Earth Sciences, China University of Geosciences, 430074 Wuhan, PR China. Tel.: +86 27 67883048.
E-mail addresses: longxiao@cug.edu.cn (L. Xiao).

0012-821X/$ - see front matter © 2004 Elsevier B.V. All rights reserved.
doi:10.1016/j.epsl.2004.10.002

1. Introduction

The Emeishan continental flood basalt province, in Yunnan, Sichuan and Guizhou provinces, SW China, has been recognized as part of the Emeishan large igneous province (ELIP) [1–4]. However, the origin of the Emeishan flood basalt is not well understood, despite numerous geochemical studies that suggest a mantle plume origin, but the role of such a mantle plume in generating basaltic magmas is not clear. In addition, the involvement of lithospheric mantle and continental crust has not been satisfactorily evaluated [3,5,6].

It is generally accepted that continental flood basalt (CFB) may be sourced from both mantle plume [3,7,8] and the subcontinental lithospheric

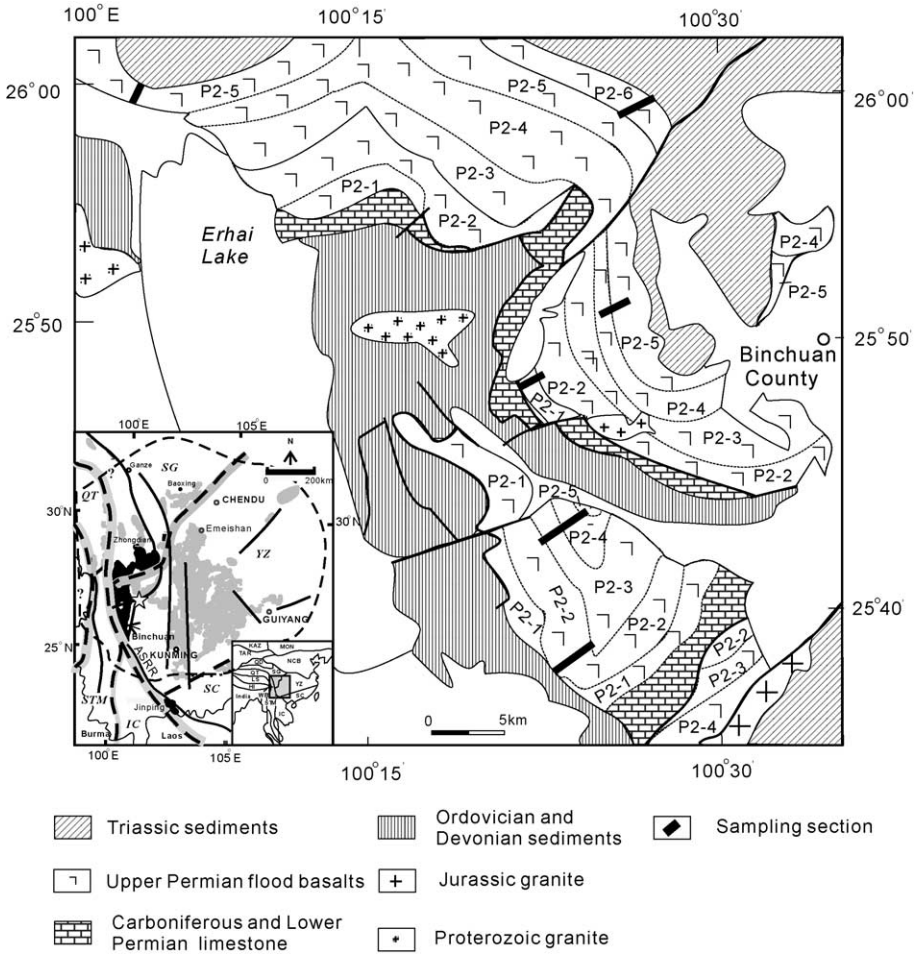

Fig. 1. Geological map and sampling locations of Binchuan area. P2-1, P2-2, P2-3, P2-4, P2-5 and P2-6 are subunits of the Emeishan flood basalts. Due to the limitations of rock exposure, sampled sections were chosen as shown by thick bars. The star shows the postulated center of the Emeishan mantle plume impact. The dashed line illustrates the assumed extent of the ELIP [4]. Inset is a schematic map showing the distribution of the Late Permian volcanic successions and subdivisions of the ELIP (gray and black areas indicate HT basalts and LT+HT subdivisions, respectively, after Xiao et al. [4]. Major terranes are: SC=South China Block; YZ=Yangtze Craton; SG=Songpan–Ganze Accretionary Complex; QT=Qiangtang; STM=San–Thai–Malay; IC=Indochina; WB=West Burma; HI=Himalayan; LS=Lhasa; QD=Qaidam; TAR=Tarim; KAZ=Kazkhstan; MON=Mongolia; NCB=North China Block).

mantle [9–12], although physical modelling supports melts derived from the sub-lithospheric mantle [13–15].

Crustal signatures of some CFB may reflect either their crustal-modified source, or input of crustal components en route to the surface. In the former case, crustal components are normally regarded as located in the subcontinental lithospheric mantle (e.g. [9,10,12,16]); arc- or back arc-like mantle sources [17,18]. Crustal material input could result from either crustal contamination of lithosphere-derived melts or asthenosphere-derived magmas [15,16,19,20]. However, there is debate about the factors that can cause lithosphere to melt and produce voluminous mafic magmas [14]. Most geologists believe that melting of relatively refractory lithosphere mantle should satisfy the following geological conditions: (1) anomalously high temperature of the mantle (lithosphere is more refractory than asthenosphere); (2) extension and thinning of lithosphere to cause decompression melting [21]; and (3) the presence of volatile that can lower the solidus [22].

The Emeishan continental flood basalts (ECFB) comprise both low-Ti (LT) and high-Ti (HT) basalts [3,4], which display spatial and temporal variations [4]. Plume-impact doming and crustal uplift occurred in the Binchuan–Miyi region, but in the western sector of the ELIP there appears to be no marked uplift and lithosphere extension [23]. However, extension could have occurred at the western Yangtze craton margin, which resulted in rifting and opening of the Ganze-Litang Ocean that separated the Zhongza micro-block from the Yangtze craton [2,24,25]. The western Yangtze craton was an active margin during the late Proterozoic [26–29] that could have resulted in enrichment and metasomatism of the continental lithosphere mantle by the action of slab-derived fluids. This geological setting may have played an important role on rock type variations, both temporally and spatially. This is discussed in Section 7.

This study provides new major, trace elements and Sr–Nd isotopic data of the basaltic rocks collected from a composite section at Binchuan. Together with new oxygen isotope composition of phenocrysts from the LT basalts, these data allow us to identify three rock types, LT1, LT2 and HT, to discuss the bearing of their temporal variation, and to characterize their source. Finally, we address the geodynamic implications of plume–lithosphere interaction based on the genetic relationship of the HT, LT1 and LT2 magmas.

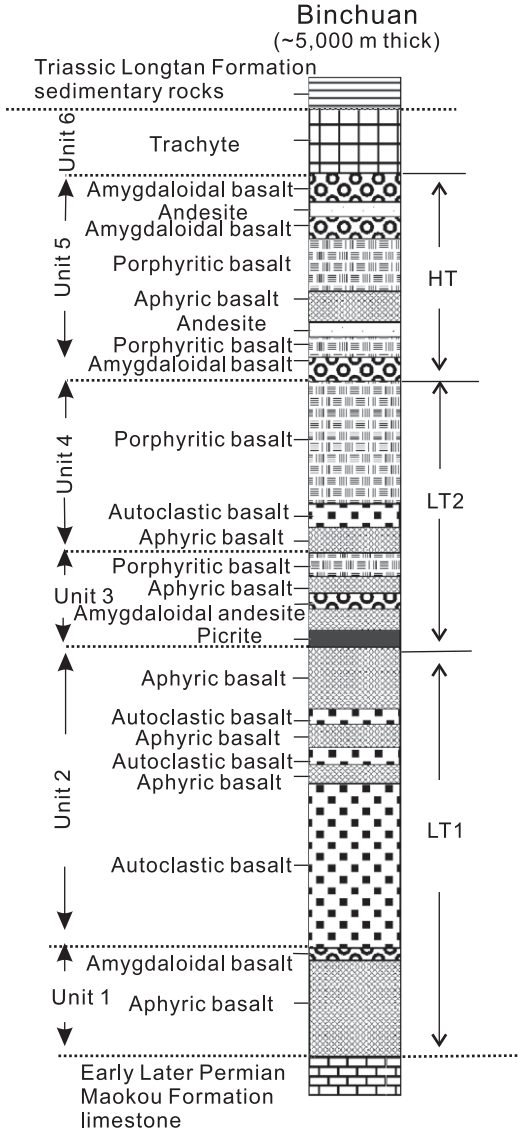

Fig. 2. Composite stratigraphy and sampling column at Binchuan area. Relative stratigraphic locations are shown in Fig. 1. Magma types of studied samples in the volcanic section are shown. Each shaded part represents an individual lava flow.

Table 1
Major oxides and trace-element abundances of late Permian basalts from Binchuan area

LT1														
Sample	SC-2	SC-6	SC-7	SC-8	SC-9	WL-1	WL-2	WL-3	WL-4	WL-5	WL-6	WL-7	WL-8	WL-9
wt.%														
SiO_2	49.91	51.44	43.55	49.85	47.82	51.29	50.07	53.14	47.87	51.51	52.1	47.62	47.01	47.98
TiO_2	1.59	1.38	1.49	1.64	1.72	1.9	1.98	2.12	1.47	1.29	1.31	1.53	1.54	1.5
Al_2O_3	13.65	14.37	16.24	14.92	14.36	12.49	13.35	12.4	14.34	12.56	12.88	13.1	12.52	12.39
Fe_2O_3	1.68	1.5	1.21	1.73	1.69	1.97	1.94	1.8	1.59	1.54	1.47	1.62	1.61	1.58
FeO	8.57	7.67	6.17	8.83	8.64	11.16	11	9.2	8.12	8.73	7.52	8.28	8.23	8.05
MnO	0.16	0.14	0.13	0.16	0.16	0.18	0.18	0.17	0.15	0.14	0.13	0.15	0.15	0.18
MgO	8.21	6.98	4.78	7.68	6.11	6.55	6.49	5.65	7.92	8.47	6.4	9.11	9.33	9.2
CaO	10.64	8.73	22.36	8.9	13.39	10.1	10.22	8.1	11.17	11.81	11.45	11.89	12.17	11.34
Na_2O	2.19	3.85	0.16	3.49	1.9	2.18	2.3	4.96	2.43	2	1.93	1.7	1.47	2.16
K_2O	0.62	0.75	0.03	0.62	0.4	0.62	0.62	0.29	0.43	0.94	0.37	0.45	1.15	0.9
P_2O_5	0.17	0.16	0.18	0.18	0.16	0.14	0.16	0.39	0.12	0.16	0.1	0.12	0.13	0.13
LOI	2.09	3.33	4	2.69	4.14	1.94	1.72	2.56	5.05	2.13	4.85	5.1	4.23	3.74
Total	99.5	100.34	100.34	100.72	100.54	100.53	100.97	100.82	100.71	99.89	100.55	100.71	99.58	99.19
Mg#	63	62	58	61	56	51	52	53	64	64	61	66	67	67
ppm														
Ba	217	176	16	190	44	81	65	42	135	368	85	119	353	231
Rb	22	18	1	22	10	11	10	5	11	26	9	13	28	21
Sr	464	357	39	464	119	130	129	179	265	198	170	162	338	272
Y	26	29	26	28	26	30	32	32	25	24	22	25	23	24
Zr	151	180	117	148	119	123	127	158	127	114	108	133	129	131
Nb	12.8	12.7	11.7	13.1	8.1	7.9	8	20.5	11.2	10.1	10	12	12	12
Th	3.3	6.2	2	3	2.1	0.9	0.9	1.9	2.4	2.3	1.9	2.7	2.6	2.6
Ga	19	21	28	19	27	20	22	16	20	18	20	20	18	19
Zn	82	79	48	93	101	107	104	98	91	78	77	86	78	84
Cu	60	24	21	37	95	191	211	209	40	74	46	81	79	81
Ni	118	90	46	53	82	118	110	62	131	154	120	193	195	178
V	290	218	235	281	235	390	406	269	304	305	260	295	293	292
Cr	372	356	266	391	339	263	272	114	314	403	266	509	541	499
Hf	3.51	4.19	2.79	3.4	2.93	3.1	3.19	3.68	3.02	2.66	2.54	3.09	3.13	3.12
Cs	2.39	0.07	0.19	0.44	0.32	0.32	0.25	0.1	0.77	0.37	0.28	0.52	0.73	0.73
Sc	36.57	26.76	29.04	34.61	27.02	37.7	40.19	27.06	31.25	31.13	27.4	37.41	37.01	34.86
Ta	0.77	0.82	0.68	0.81	0.52	0.5	0.5	1.12	0.7	0.62	0.58	0.72	0.73	0.77
Co	46.3	38.74	31.93	44.34	45.86	47.53	46.7	38.7	45.31	46.74	38.8	51.2	49.86	48.57
U	0.74	1.39	0.46	0.68	0.49	0.28	0.3	0.47	0.61	0.59	0.46	0.63	0.63	0.64
La	15.38	21.01	9.86	15.17	9.9	5.51	7.28	16.13	14.6	14.23	11.32	13.12	11.4	12.85
Ce	32.8	43.1	23.7	32.3	22.38	15.35	17.3	33.84	29.54	29.25	23.35	27.38	24.61	26.71
Pr	4.49	5.58	3.53	4.42	3.37	2.54	2.76	4.73	4.07	4.01	3.3	3.79	3.5	3.74
Nd	19.42	22.7	16.16	19.37	16.26	13.28	14.12	21.19	17.97	17.48	14.41	16.44	15.93	16.84
Sm	4.55	5.07	4.08	4.72	4.23	4.07	4.22	5.16	4.33	4.08	3.5	4.03	4	4.14
Eu	1.48	1.58	1.29	1.51	1.57	1.43	1.59	1.78	1.47	1.42	1.25	1.41	1.34	1.39
Gd	4.93	5.26	4.7	5.21	5.05	5.34	5.51	5.88	4.84	4.56	3.95	4.49	4.61	4.56
Tb	0.77	0.85	0.75	0.82	0.78	0.88	0.93	0.93	0.77	0.71	0.64	0.72	0.71	0.74
Dy	4.35	4.91	4.34	4.68	4.51	5.32	5.5	5.4	4.33	3.99	3.65	4.18	4.21	4.21
Ho	0.82	0.95	0.83	0.89	0.82	1.03	1.05	1.05	0.83	0.75	0.7	0.78	0.78	0.77
Er	2.19	2.58	2.15	2.37	2.27	2.92	2.99	2.9	2.25	1.94	1.84	2.06	2.16	2.14
Tm	0.31	0.39	0.32	0.35	0.31	0.41	0.42	0.4	0.32	0.28	0.27	0.3	0.3	0.3
Yb	1.93	2.37	1.94	2.17	1.9	2.55	2.64	2.52	1.98	1.7	1.63	1.86	1.87	1.95
Lu	0.3	0.38	0.31	0.35	0.28	0.38	0.4	0.38	0.3	0.27	0.26	0.29	0.28	0.3
Ti/Y	422	281	375	391	409	390	386	427	388	343	372	445	422	417
REE	93.72	116.73	73.96	94.33	73.63	61.01	66.71	102.29	87.6	84.67	70.07	80.85	75.7	80.64
Th/Nb	0.26	0.49	0.17	0.23	0.26	0.11	0.11	0.09	0.21	0.23	0.19	0.23	0.22	0.22
Sm/Yb	2.36	2.14	2.10	2.18	2.23	1.60	1.60	2.05	2.19	2.40	2.15	2.17	2.14	2.12
Nb/U	17.30	9.14	25.43	19.26	16.53	28.21	26.67	43.62	18.36	17.12	21.74	19.05	19.05	18.75
Zr/Nb	11.80	14.17	10.00	11.30	14.69	15.57	15.88	7.71	11.34	11.29	10.80	11.08	10.75	10.92
La/Nb	1.20	1.65	0.84	1.16	1.22	0.70	0.91	0.79	1.30	1.41	1.13	1.09	0.95	1.07
Ba/Nb	16.95	13.86	1.37	14.50	5.43	10.25	8.13	2.05	12.05	36.44	8.50	9.92	29.42	19.25

Mg#=100Mg/(Mg+Fe).

					LT2										Picrite
WL-11	WL-13	WL-16	WL-17	WL-18	WL-23	WL-25	WL-27	WL-28	WL-31	WL-34	WL-35	WL-36	WL-37	WL-39	WL-38
51.41	47.04	50.54	50.43	50.86	51.61	48.26	51.08	50.46	49.95	49.14	55.92	52.5	47.88	46.76	44.06
1.23	1.41	1.42	1.4	1.48	1.7	1.53	1.56	1.65	2.23	1.78	1.72	1.85	2.28	2.03	0.9
11.27	12.79	13.98	14.69	14.02	12.38	14.8	12.96	14.54	11.65	13.98	11.74	12.93	13.95	14.98	8.3
1.41	1.64	1.63	1.57	1.66	2.04	2.01	1.84	1.87	1.84	2.07	1.67	1.7	1.94	1.96	1.67
7.18	8.36	8.32	7.99	8.48	10.39	10.26	9.36	9.54	9.37	10.53	9.46	8.66	9.87	10.02	8.49
0.14	0.15	0.15	0.15	0.17	0.18	0.21	0.14	0.17	0.17	0.15	0.13	0.16	0.17	0.2	0.16
7.76	8.46	6.75	6.89	8.11	6.23	5.78	5.44	5.56	5.22	5.36	4.48	3.8	5.49	5.48	22
12.79	12.42	9.76	10.1	9.45	8.18	11.04	8.88	5.38	13.97	7.66	8.48	13.05	10.89	10.68	8.54
0.82	1.6	3.12	2.71	3.22	4.15	2.94	4.66	4.97	0.94	3.69	4.41	0.05	3.49	2.59	0.87
0.42	0.51	0.93	1.55	0.82	0.96	1.24	0.94	0.3	0.16	1.97	0.17	0.03	0.14	2.06	0.54
0.11	0.12	0.14	0.14	0.16	0.19	0.18	0.3	0.45	0.43	0.42	0.4	0.34	0.34	0.62	0.11
4.49	4.55	3.72	3.1	2.5	2.89	1.72	2.68	4.39	3.88	4.12	2.09	5.14	4.32	2.27	4.37
99.08	99.09	100.49	100.74	100.95	100.93	100	99.87	99.16	99.85	100.92	100.67	100.26	100.82	99.67	100.05
66	65	59	61	63	52	50	51	51	50	48	46	44	50	50	82
99	149	162	319	114	477	291	199	73	25	823	35	21	26	951	132
9	14	24	49	40	23	33	17	8	3	78	4	2	3	65	33
159	198	184	450	635	379	219	217	540	56	756	123	52	99	725	165
21	23	27	24	27	31	31	25	25	32	24	25	27	32	27	16
108	123	135	133	146	105	126	106	113	158	116	125	134	168	125	78
10	11	11	11	12	11	11	13	18	21	19	16	18	22	27	8
2.2	2.4	3.5	3.5	3.6	1.1	2	1.4	1.7	2	1.5	1.5	1.7	2	1.4	1.6
19	22	18	17	18	15	21	15	19	28	14	16	27	28	21	12
69	82	97	71	85	113	104	113	95	94	97	81	91	116	121	85
72	132	26	63	12	24	155	133	48	162	185	136	174	248	343	96
156	187	33	33	34	72	76	68	67	63	61	46	64	68	62	974
254	284	266	277	279	369	307	301	323	280	317	237	240	329	338	194
419	503	130	128	131	71	60	30	41	108	25	86	90	112	32	18
2.6	2.87	3.2	3.2	3.36	2.62	2.96	2.57	2.65	3.75	2.82	2.94	3.15	3.95	2.75	1.83
0.51	0.45	0.13	0.34	0.43	0.44	0.36	0.25	0.38	0.08	1.07	0.37	0.34	0.14	4.03	3.04
29.56	33.34	31.62	31.43	33.25	40.51	33.31	27.8	24.24	25.41	24.57	21.25	20.64	26.45	19.43	24.89
0.6	0.68	0.68	0.67	0.7	0.67	0.66	0.71	0.92	1.14	0.99	0.91	0.98	1.19	1.4	0.46
42.03	47.97	40.53	39.35	45.13	50.2	47.94	41.16	44.75	37.82	43.29	31.06	35.55	40.69	43.4	83.53
0.53	0.56	0.8	0.81	0.94	0.24	0.54	0.33	0.41	0.48	0.4	0.34	0.35	0.53	0.35	0.51
10.97	12.12	15.52	15.05	14.73	7.05	9.69	8.21	10.94	14.4	9.92	11.69	13.45	14.29	12.01	7.25
23.03	25.33	31.21	31.45	31.22	18.52	21.13	18.76	23.65	30.41	21.49	24.81	27.6	31.19	25.59	15.31
3.22	3.48	4.28	4.3	4.34	2.9	3.07	2.87	3.32	4.28	3.15	3.47	3.96	4.47	3.6	2.15
14.27	15.64	18.91	18.64	18.67	13.83	14.45	13.46	15	19.55	14.67	15.83	18.03	20.29	16.16	9.65
3.53	3.85	4.42	4.37	4.46	3.82	3.92	3.63	3.7	4.99	3.71	3.97	4.38	5.01	4.03	2.4
1.25	1.34	1.41	1.39	1.22	1.3	1.39	1.16	1.29	1.63	1.25	1.35	1.59	1.68	1.39	0.79
3.92	4.29	4.85	4.71	4.79	4.71	4.95	4.4	4.32	5.67	4.6	4.64	5.08	5.76	4.84	2.87
0.63	0.69	0.76	0.75	0.77	0.83	0.83	0.7	0.71	0.93	0.73	0.72	0.8	0.93	0.78	0.46
3.67	3.88	4.39	4.28	4.44	4.9	5.06	4.12	4.13	5.43	4.35	4.26	4.71	5.44	4.5	2.7
0.68	0.75	0.82	0.79	0.83	0.99	1.01	0.79	0.8	1.03	0.82	0.8	0.88	1.03	0.9	0.52
1.89	1.95	2.34	2.25	2.22	2.69	2.87	2.22	2.13	2.82	2.28	2.28	2.48	2.88	2.38	1.39
0.26	0.29	0.32	0.31	0.33	0.4	0.41	0.3	0.32	0.4	0.32	0.32	0.35	0.42	0.36	0.2
1.64	1.77	2.03	1.95	2.06	2.49	2.64	1.92	1.95	2.57	2.05	1.98	2.18	2.63	2.21	1.27
0.25	0.27	0.31	0.31	0.32	0.4	0.41	0.3	0.31	0.39	0.32	0.31	0.33	0.41	0.35	0.2
360	423	334	342	344	389	315	396	447	427	451	435	417	441	490	350
69.21	75.65	91.57	90.55	90.4	64.83	71.83	62.84	72.57	94.5	69.66	76.43	85.82	96.43	79.1	47.16
0.22	0.22	0.32	0.32	0.30	0.10	0.18	0.11	0.09	0.10	0.08	0.09	0.09	0.09	0.05	0.20
2.15	2.18	2.18	2.24	2.17	1.53	1.48	1.89	1.90	1.94	1.81	2.01	2.01	1.90	1.82	1.89
18.87	19.64	13.75	13.58	12.77	45.83	20.37	39.39	43.90	43.75	47.50	47.06	51.43	41.51	77.14	15.69
10.80	11.18	12.27	12.09	12.17	9.55	11.45	8.15	6.28	7.52	6.11	7.81	7.44	7.64	4.63	9.75
1.10	1.10	1.41	1.37	1.23	0.64	0.88	0.63	0.61	0.69	0.52	0.73	0.75	0.65	0.44	0.91
9.90	13.55	14.73	29.00	9.50	43.36	26.45	15.31	4.06	1.19	43.32	2.19	1.17	1.18	35.22	16.50

(continued on next page)

Table 1 (*continued*)

HT															
Sample	DY-3	DY-5	RY-1	RY-3	RY-4	RY-5	RY-6	RY-7	RY-8	RY-9	RY-10	RY-11	WL-19	WL-20	WL-21
wt.%															
SiO_2	49.32	49.81	42.08	51.86	50.86	48.34	48.24	43.38	45.68	61.3	51.09	50.46	49.64	50.55	57.86
TiO_2	3.67	3.97	5.21	4.07	4.26	4.34	4.25	4.59	4.5	3.58	4.3	4.63	3.63	4.58	3.91
Al_2O_3	13.24	12.8	14.81	12.29	12.46	13.25	13.92	14.78	14.93	11.55	11.92	13.93	12.76	12.28	10.8
Fe_2O_3	2.06	2.42	2.5	2.01	2.04	2.15	2.02	2.11	2.13	1.74	2.27	1.93	2.15	2.01	1.78
FeO	11.67	12.36	12.77	10.25	10.42	10.95	10.31	10.75	10.88	8.88	11.56	9.85	10.95	10.26	9.1
MnO	0.23	0.21	0.16	0.17	0.18	0.16	0.16	0.22	0.23	0.1	0.28	0.3	0.23	0.18	0.13
MgO	3.52	4.8	5.34	4.76	3.83	4.86	5.07	6.8	6.88	2.26	6.04	5.73	4.86	4.48	2.54
CaO	8.43	9.16	8.68	6.76	8.69	8.06	5.15	7.12	5.5	2.78	3.81	4.34	9.86	6.77	10.33
Na_2O	2.49	2.38	4.12	3.78	3.23	3.45	4.76	3.09	4.74	2.87	2.68	4.26	2.67	3.63	1.07
K_2O	1.75	0.39	0.05	0.05	0.9	2.28	0.71	1.33	0.33	2.02	0.43	0.35	1.06	1.74	0.08
P_2O_5	0.46	0.42	0.47	0.41	0.31	0.42	0.43	0.48	0.41	0.31	0.38	0.43	0.38	0.47	0.43
LOI	3.1	1.69	4.09	3.14	2.61	1.92	4.41	4.39	3.94	2.58	4.28	3.91	1.55	2.39	2.46
Total	99.94	100.44	100.35	99.59	99.82	100.2	99.49	99.1	100.94	99.99	99.1	100.16	99.76	99.38	100.53
Mg#	35	41	43	46	40	44	47	53	53	31	48	51	44	44	33
ppm															
Ba	100	202	26	15	339	852	218	517	122	401	150	123	386	448	24
Rb	32	9	1	1	11	70	15	36	6	62	12	8	21	46	2
Sr	599	293	167	286	439	469	424	287	337	170	304	287	413	353	369
Y	45	53	52	41	33	41	42	48	38	33	38	48	47	51	44
Zr	474	310	543	378	348	403	402	436	416	322	348	403	287	436	364
Nb	60	25	68	48	52	51	52	56	53	42	46	49	27	54	45
Th	11.7	3.8	8.8	5.6	5.2	6.1	6.1	6.5	6.2	4.9	5	5.5	4	7.7	6.2
Ga	27	28	26	22	25	19	23	24	27	14	28	24	24	27	21
Zn	138	166	184	116	112	109	123	152	138	92	143	131	120	136	102
Cu	255	643	213	320	37	71	162	260	64	386	5	336	396	285	292
Ni	34	106	55	56	52	65	74	74	78	62	58	51	54	63	71
V	292	451	413	366	378	383	380	413	382	219	411	432	414	396	280
Cr	57	51	20	72	72	94	106	95	104	106	49	37	55	81	66
Hf	10.31	7.15	11.34	8.02	7.85	8.72	8.61	9.38	8.99	7.05	7.67	8.79	6.45	9.38	7.95
Cs	0.36	0.19	0.44	0.57	0.63	12.11	2.93	5.3	2.14	16.47	4.59	2.4	0.74	0.33	0.06
Sc	20.25	28.22	35.93	27.69	29.09	30.28	30.22	32.14	31.14	24.17	31.84	33.69	29.08	28.27	23.59
Ta	3.58	1.47	4.14	3	3.14	3.17	3.14	3.44	3.25	2.57	2.88	3.02	1.59	3.35	2.74
Co	33.66	44.69	52.89	37.82	34.47	36.8	42.63	48.63	46.58	26.89	45.45	49.4	38.61	37.65	28.13
U	2.55	1.05	1.4	1.47	1.25	1.29	1.48	2.36	0.93	0.63	1.19	1.44	1.04	1.87	1.27
La	61.29	22.09	61.23	47.68	40.42	41.14	46.52	58.61	42.44	35.15	36	35.9	21.69	46.99	38.87
Ce	126.7	51.34	137.9	96.33	86.88	93.48	102.3	125.8	91.28	78.15	84.54	87.86	51.21	99.95	83.76
Pr	15.97	7.67	18.35	12.78	11.55	12.74	13.39	16.48	12.03	10.07	11.88	12.57	7.34	13.56	11.2
Nd	63.18	35.71	73.9	52.4	47.5	53.45	54.97	65.9	51.35	42.27	50.31	53.93	33.16	56.04	46.88
Sm	11.72	8.99	14.02	10.19	9.16	10.63	10.49	12.32	10.22	8.25	10.02	11.24	8.17	11.42	9.68
Eu	3.38	2.8	3.72	3.08	2.86	3.1	2.87	3.24	3.18	2.62	3.07	3.31	2.66	3.28	2.7
Gd	10.45	10.04	12.1	9.22	8.04	9.56	9.53	10.88	9.03	7.88	9.01	10.56	9.07	10.77	9.35
Tb	1.57	1.63	1.76	1.36	1.19	1.44	1.43	1.66	1.35	1.15	1.36	1.59	1.44	1.65	1.43
Dy	8.29	9.23	9.21	7.31	6.19	7.55	7.63	8.87	7.18	6.03	7.17	8.47	8.14	8.87	7.55
Ho	1.48	1.7	1.67	1.31	1.09	1.35	1.37	1.62	1.29	1.08	1.27	1.51	1.51	1.62	1.38
Er	4.07	4.68	4.33	3.45	2.8	3.47	3.65	4.31	3.29	2.76	3.25	3.92	3.96	4.23	3.57
Tm	0.53	0.65	0.6	0.48	0.39	0.48	0.51	0.62	0.46	0.38	0.46	0.54	0.57	0.6	0.5
Yb	3.31	4	3.62	2.92	2.38	2.9	3.03	3.7	2.78	2.22	2.68	3.26	3.51	3.64	3.05
Lu	0.49	0.61	0.56	0.46	0.37	0.46	0.47	0.58	0.43	0.33	0.41	0.5	0.54	0.56	0.48
Ti/Y	506	558	673	659	867	704	689	640	769	718	747	636	510	637	600
REE	312.43	161.14	342.97	248.97	220.82	241.75	258.16	314.59	236.31	198.34	221.43	235.16	152.97	263.18	220.4
Th/Nb	0.20	0.15	0.13	0.12	0.10	0.12	0.12	0.12	0.12	0.12	0.11	0.11	0.15	0.14	0.14
Sm/Yb	3.54	2.25	3.87	3.49	3.85	3.67	3.46	3.33	3.68	3.72	3.74	3.45	2.33	3.14	3.17
Nb/U	23.53	23.81	48.57	32.65	41.60	39.53	35.14	23.73	56.99	66.67	38.66	34.03	25.96	28.88	35.43
Zr/Nb	7.90	12.40	7.99	7.88	6.69	7.90	7.73	7.79	7.85	7.67	7.57	8.22	10.63	8.07	8.09
La/Nb	1.02	0.88	0.90	0.99	0.78	0.81	0.89	1.05	0.80	0.84	0.78	0.73	0.80	0.87	0.86
Ba/Nb	1.67	8.08	0.38	0.31	6.52	16.71	4.19	9.23	2.30	9.55	3.26	2.51	14.30	8.30	0.53

2. The Emeishan large igneous province

The Emeishan large igneous province is a LIP that was broken up by the Red River Fault [4]. The ECFB is unconformable on the Mid-Permian Maokou Formation and is overlain by early Late Permian Longtan Formation or Triassic sedimentary rocks. Recent U–Pb SHRIMP dating of zircons from a diabase sill yielded an age of 259 Ma [30], which is consistent with field geological observations. Present-day exposures of ECFB are a remnant of the large igneous province that was partly destroyed and dismembered by post-volcanic tectonism [4,5]. Xiao et al. [4] argued that the ECFB extended beyond the Yangtze craton, and that basalts and mafic–ultramafic rocks that outcrop at Jinping and in the Zhongza micro-block [4,5] are also parts of the ELIP. Therefore, a revised estimate of the extent of the ELIP is in excess of 500,000 km^2 [31]. This estimate is based on studies suggesting that the location of the plume head was in the Binchuan–Miyi area, northwest of Kunming, shown in the inset of Fig. 1 [23], where the ECFB is thickest (5384 m [32]). This is further supported by the progressive eastward decrease in thickness of the ECFB recorded from this area [31].

In the last 20 years a number of studies have been conducted on the Emeishan basalts. Early ideas on the origin and petrogenesis of the ECFB include: (i) a link with the Panxi rift [26,32,33] and (ii) a mantle plume [2–6,23,34,35].

A mantle plume origin for continental flood basalts is becoming increasingly accepted by the geological community (e.g. [2,3,6,23,36]), although there is some debate on the precise roles and contribution of mantle plume and the lithosphere to the petrogenesis of the flood basalts. Xu et al. [3] classified the ECFB into two geochemical groups as high-Ti (HT) and low-Ti (LT) lavas, and proposed that both of the HT and LT basalts originated from a mantle plume. The difference between LT and HT lavas is that the former underwent more extensive crustal contamination. Song et al. [6] argued that the ECFB originated from enriched SCLM (sub-continental lithosphere mantle). Recently Xiao et al. [4] further classified the Emeishan CFB into three geochemical groups, as LT1, LT2 and HT, however their origins and geodynamics have not been resolved.

3. Sampling and analytical methods

Previous studies [3,4,32,34,37–39] suggested that the major rock type is tholeiite, which represents more than 95% of the ELIP. Volumetrically minor rock types include alkaline basalts, mafic and ultramafic intrusions, and felsic rocks. The lava succession in the western sector of the ELIP contains all of the above-mentioned rock types and is thicker than in the eastern sector. Therefore, for this study we have chosen the Binchuan area, where the volcanic succession was reported as 5384 m thick [31,32] thereby allowing a more complete and systematic sampling (Fig. 1). It is worth pointing out that this thickness was estimated without considering any tectonic thickening and might be not accurate. However, we checked key important geological contacts, such as lowermost lava contacts directly with the Middle Permian Maokou limestone with sedimentary contact, uppermost lava covered by Upper Permian or Lower Tertiary sandstone. Samples were collected mainly from these two clear contacts towards the middle of the lava succession; ensuring that sampling profiles represent the volcanic stratigraphy as accurately as possible. Rock samples were taken primarily from six road profiles traversing the western section of the ELIP, near Binchuan, Yunnan Province (Figs. 1 and 2). The complete composite section is shown in Fig. 2 and consists of six units (Fig. 2, units 1 to 6, 1:50,000 geological maps of Dayingjie and Fengyizheng, Yunnan, 1990, 1993, unpublished). To avoid missing parts of the volcanic stratigraphy, some adjacent rock units between the six subsections were also sampled thereby allowing a degree of overlap. Systematic sampling of the volcanic succession with a stratigraphic height control allows us to make a detailed geochemical assessment of the temporal evolution of these rocks. The Emeishan basalts are variably altered, and for the purpose of this study, samples with LOI greater than 3% have not been considered.

Fifty-eight basalts, three rhyolitic rocks and one picrite were analyzed in this study. The rocks were sawn into slabs and the fresh central portions were handpicked and powdered using stainless steel mill. Whole-rock abundances of major, trace and rare-earth elements were determined using ICP-AES and

ICP-MS at Guangzhou Institute of Geochemistry, Chinese Academy of Sciences (GIG-CAS). Analytical uncertainties are ±1–2% for major elements, ±5% for rare-earth elements, and ±5–10% for trace elements, respectively. The detailed analytical procedures were given in Liu et al. [40] and Xu et al. [41]. Results are presented in Table 1.

These powdered samples were also used for Sr–Nd isotopic analysis. Nd–Sr analytical techniques followed Mao et al. [42] and Liang et al. [43]. Nd–Sr isotope compositions were measured on a MC-ICPMS at GIG-CAS. The analytical errors are less than 0.005% for $^{143}Nd/^{144}Nd$ and $(^{87}Sr/^{86}Sr)_i$ ratios. Results are given in Table 2. Samples chosen for Sr–Nd isotope analysis have relatively high MgO contents (MgO>5%), in order to make them close to primary magma.

For oxygen isotope analysis, plagioclase and clinopyroxene phenocrysts were separated and then carefully handpicked under binocular microscope to avoid weathered or altered crystals. Nevertheless, most plagioclase phenocrysts show signs of slight alteration. Oxygen isotope analysis of minerals was carried out by the laser fluorination technique using a 25 W MIR-10 CO_2 laser at Laboratory for Chemical Geodynamics in the University of Science and Technology of China [44]. O_2 was directly transferred to a Delta+ mass spectrometer for the measurement of $^{18}O/^{16}O$ and $^{17}O/^{16}O$ ratios. Two reference minerals were used: $\delta^{18}O$=5.80 for UWG-2 garnet, and $\delta^{18}O$=5.20 for SCO-1 olivine. Reproducibility for repeat measurements of each standard on a given day was better than ±0.1‰ for $\delta^{18}O$.

4. Petrography and geochemistry

4.1. Petrography

The Emeishan basalts consist of various rock types. Based on field, hand specimen and optical microscopy observations, rock types and their textures are summarized in Fig. 2. The lower part of Binchuan lava succession (unit 1 and unit 2) consists mainly of aphyric and locally hyaloclastite lava. Phenocrysts in these rocks are minor and where present they are plagioclase (<3%), olivine (1–3%) and augite (1–2%). The groundmass is composed of plagioclase (30–50%), basaltic glass (30–45%) and Ti–Fe oxides (5–10%).

Middle part (unit 3 and unit 4) has more porphyritic basalts than lower part unit 1 and unit 2. Plagioclase phenocrysts in these rocks range from 2% to 10%; minor phenocrysts are olivine (1–2%) and augite (1–3%). The porphyritic and aphyric basalts of Unit 3 are interlayered. Some basalts exhibit a glomeroporphyritic texture containing bunches of greater than 5 mm plagioclase phenocrysts. The composition of ground is similar to unit 1 and unit 2.

Upper part unit 5 basalts have higher phenocryst contents than those in the lower part. The dominant

Table 2
Rb–Sr and Sm–Nd isotopic ratios and abundances for the Emeishan flood basalts from Binchuan and Jinping areas

Rock type	Sample	Rb	Sr	$(^{87}Sr/^{86}Sr)m$	$(^{87}Sr/^{86}Sr)_i$	Sm	Nd	$(^{143}Nd/^{144}Nd)m$	$(^{143}Nd/^{144}Nd)i$	$\varepsilon Nd(t)$
HT	RY-5	70	439	0.706552 11	0.704913	10.63	47.5	0.512478 13	0.512256	−1.17
	RY-6	15	424	0.706318 11	0.705962	10.49	54.97	0.512501 13	0.512312	−0.08
	RY-8	6	337	0.706217 11	0.706044	10.22	51.35	0.512477 15	0.51228	−0.71
	RY-10	12	304	0.706743 12	0.70632	10.02	50.31	0.512535 14	0.512338	0.43
	RY-11	8	287	0.706721 12	0.706436	11.24	53.93	0.512540 12	0.512334	0.34
LT2	WL-25	33	219	0.706553 12	0.704994	3.917	14.45	0.512524 14	0.512255	−1.18
	WL-27	17	217	0.706043 12	0.705258	3.633	13.46	0.512544 14	0.512277	−0.76
	WL-28	8	540	0.706226 12	0.706068	3.698	15	0.512542 16	0.512298	−0.35
LT1	SC-2	252	464	0.706819 14	0.706325	4.546	19.42	0.512387±12	0.512155	−3.14
	WL-4	11	265	0.706849 9	0.706422	4.33	17.97	0.512470±13	0.512232	−1.64
	WL-6	9	170	0.706909 14	0.706343	3.502	14.41	0.512539±15	0.512299	−0.34
	WL-16	24	183	0.708135 11	0.706775	4.416	18.91	0.512354 14	0.512123	−3.76
	WL-18	40	634	0.707343 11	0.706693	4.46	18.67	0.512393 14	0.512156	−3.12

phenocryst is plagioclase (3–15%). Minor phenocryst is augite (1–3%). The groundmass is predominantly composed of plagioclase (50–60%), microlite feldspars (35–45%) and Ti–Fe oxides (3–5%). Three thin layers (0.5 to 3 m thick) of rhyolitic tuff are intercalated within this unit. The top of the succession is composed of trachyte, which contains albite phenocryst (1–5%) in an aphanitic groundmass. This paper focuses on the study of basaltic rocks only.

4.2. Geochemistry

4.2.1. Rock types and stratigraphic variation

As described above, the lower part of the lava succession consists mainly of aphyric basalts that contain olivine–plagioclase–augite phenocrysts, while the upper part is dominated of plagioclase phenocryst. This variation may suggest a chemical evolution of the magmas.

The use of lithogeochemistry has become important in defining lithostratigraphic subdivisions of continental flood basalt provinces of all ages (e.g. [45–48]), thereby providing a basis for stratigraphic correlation and an essential geochemical evolutionary framework that allow the construction of petrogenetic models [49]. Xu et al. [3] divided the Emeishan basalts into two compositional groups, mainly based on their Ti/Y ratios and TiO_2 contents. They are high-Ti group (HT; with Ti/Y>500 and TiO_2>2.5 wt.% contents) and the low-Ti group (LT; with Ti/Y<500 and TiO_2<2.5 wt.% contents).

According to this classification scheme, the lower part of the section including units 1 to 4 are LT basalts, which have a thickness in excess of 3000 m, whereas unit 5, in the upper part of the section, is represented by HT basalts. Other significant geochemical differences among the LT basalts, such as Mg#(Mg#=100 Mg/(Mg+Fe^{2+}) with Fe^{3+}/Fe^{2+}=0.15), REE (rare earth element), Sm/Yb, Nb/La, Zr/Nb, Th/Nb, etc., allow us to further divide the LT basalts into two subgroups as LT1 and LT2 [4]. Their geochemical parameters are listed in Table 1 and Fig. 3. Fig. 4 shows that in the Binchuan area, Ti/Y in the basalts is correlated with Mg#, Sm/Yb and $\varepsilon Nd(t)$. In general, the HT basalts have higher Sm/Yb ratios and $\varepsilon Nd(t)$ than the LT1 and LT2 basalts. The LT1 basalts have higher Mg# compared to the LT2 and HT basalts (Fig. 4a), and the LT1 basalts have higher Sm/Yb ratios than that of

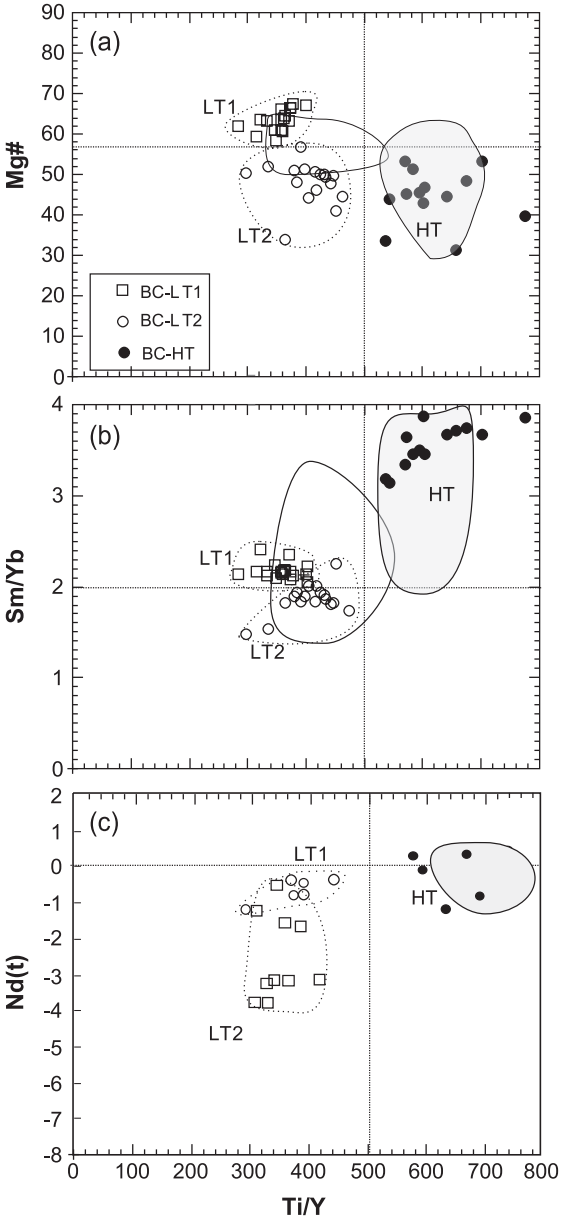

Fig. 3. Diagram showing variation of Mg#, Sm/Yb and $\varepsilon Nd(t)$ against Ti/Y for the Emeishan basalts from Binchuan. Data for Jinping basalts (JP-LT and JP-HT) are after Xiao et al. [50]. Shaded area and solid-line defined area are from Xu et al. [3], which represent HT and LT, respectively.

LT2 (Fig. 3b). Additional difference can also be seen in their trace element pattern (see Figs. 6 and 12). These parameters are consistent with those from other areas of the ELIP [3].

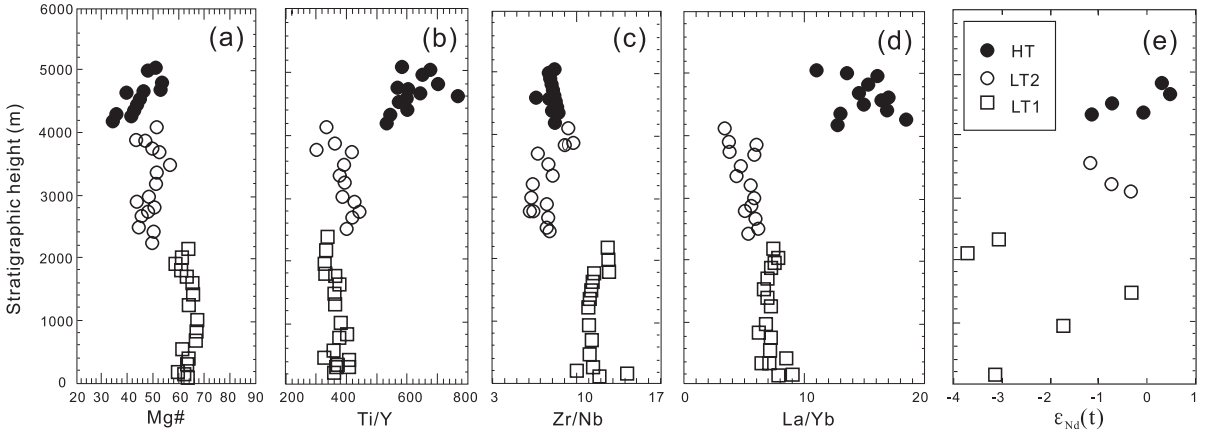

Fig. 4. Vertical variation of geochemical parameters for the Emeishan basalts. At the height of around 2200 m Zr/Nb and $\varepsilon Nd(t)$ show remarkable changes, and above 4000 m, Ti/Y and La/Nb ratios are much higher than lower part corresponding to variations of Mg#.

4.2.2. Major and minor elements

The basalts from Binchuan area display a wide variation in major element composition (Table 1). In general, the HT lavas (Mg#=53–31) are more evolved than the LT basalts (Mg#=67–44), in which the LT1 basalts have higher Mg# (67–51) than the LT2 basalts (Mg#=54–44) (Table 1). A notable feature is the temporal increase of Mg# in LT1 and decreases in LT2 (Fig. 4).

Relationships between Mg# and major elements are shown in Fig. 5. Generally, for the LT basalts negative correlations are recorded between Mg# and Al_2O_3, and Fe_2O_3 contents, whereas positive correlations between Mg# and Al_2O_3 and TiO_2, and negative correlations between Mg# and SiO_2 can be seen in the HT basalts. HT basalts show consistent fractional trends for all elements, while regression lines for LT1 and LT2 basalts show notable difference between them, particularly for SiO_2, Al_2O_3 and Nb. The HT basalts have higher TiO_2, Nb and Zr contents than the LT basalts, and the LT1 basalts have relatively higher Cr and Ni, and lower Nb contents than the LT2 basalts. In plots of Mg# vs. Ni, Cr, Zr and Nb, Mg# increases with the Ni and Cr contents and decrease with Nb in all LT basalts (Fig. 5).

4.2.3. Incompatible trace elements

The HT basalts have higher Th, U, Hf and REE contents than that of the LT basalts (Table 1). The REE patterns are shown in Fig. 6a,b and c. The HT basalts have higher total REE contents (REE=198–315 ppm) and stronger differentiation ((La/Yb)N=9–12) than the LT basalts (REE=62–116 ppm; (La/Yb)N=3–6). REE variations are also noted between the LT1 and the LT2 basalts. The LT2 basalts display a flatter pattern and lower light REE contents (La/Yb)N=3–4) than the LT1 basalts. The LT1 basalts generally have lower Sm/Yb and Nb/U, and higher Th/Nb ratios than the HT basalts (Table 1). In primitive-mantle normalized spider-diagrams (Fig. 6d,e,f), both the LT2 and the HT basalts differ from MORB (mid-ocean ridge basalt), but are generally similar to OIB (ocean island basalt, also see Fig. 12). The HT basalts are comparable with OIB, are strongly enriched in incompatible trace elements and display Sr and P negative anomalies. The LT1 basalts have pronounced Th and U positive anomalies, Nb and Ta negative anomalies and Sr and P negative anomalies, which may be related to plagioclase and apatite fractionation. The LT2 basalts display Nb, Ta, Sr, Rb and Ba positive anomalies (except for sample WL-28).

4.2.4. Sr and Nd isotopes

Sr and Nd isotopic ratios and abundances are listed in Table 2. The initial isotopic ratios were corrected to 259 Ma [30]. In the ($^{87}Sr/^{86}Sr)_i$ vs. $\varepsilon Nd(t)$ correlation diagram (Fig. 7), the Emeishan basalts define a trend that lies near the "mantle

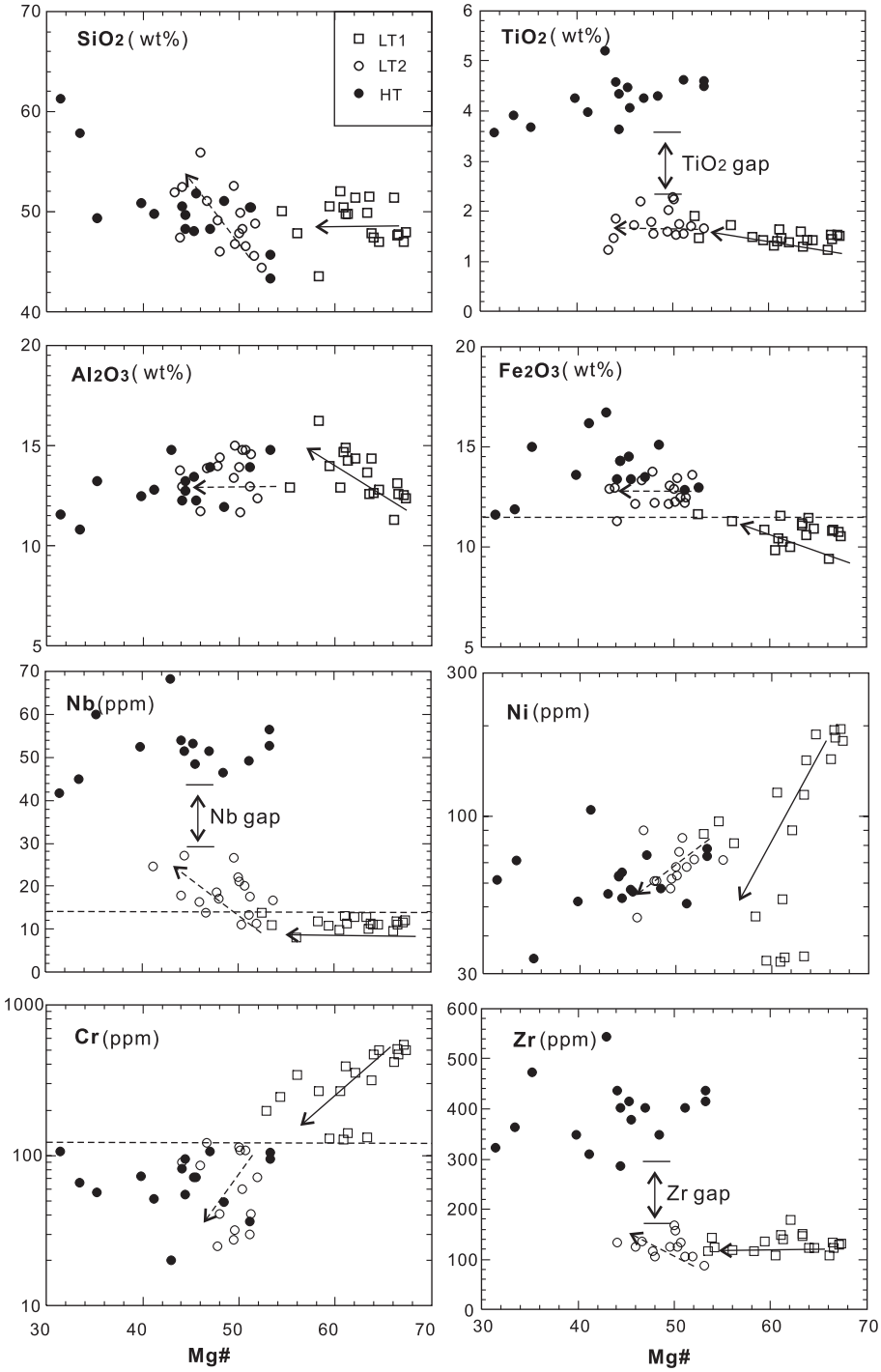

Fig. 5. Variation of SiO_2, TiO_2, Al_2O_3, Fe_2O_3, Ni, Zr, Cr and Nb vs. Mg# for the Emeishan basalts. Solid and dashed arrows represent regression lines for LT1 and LT2 basalts, respectively.

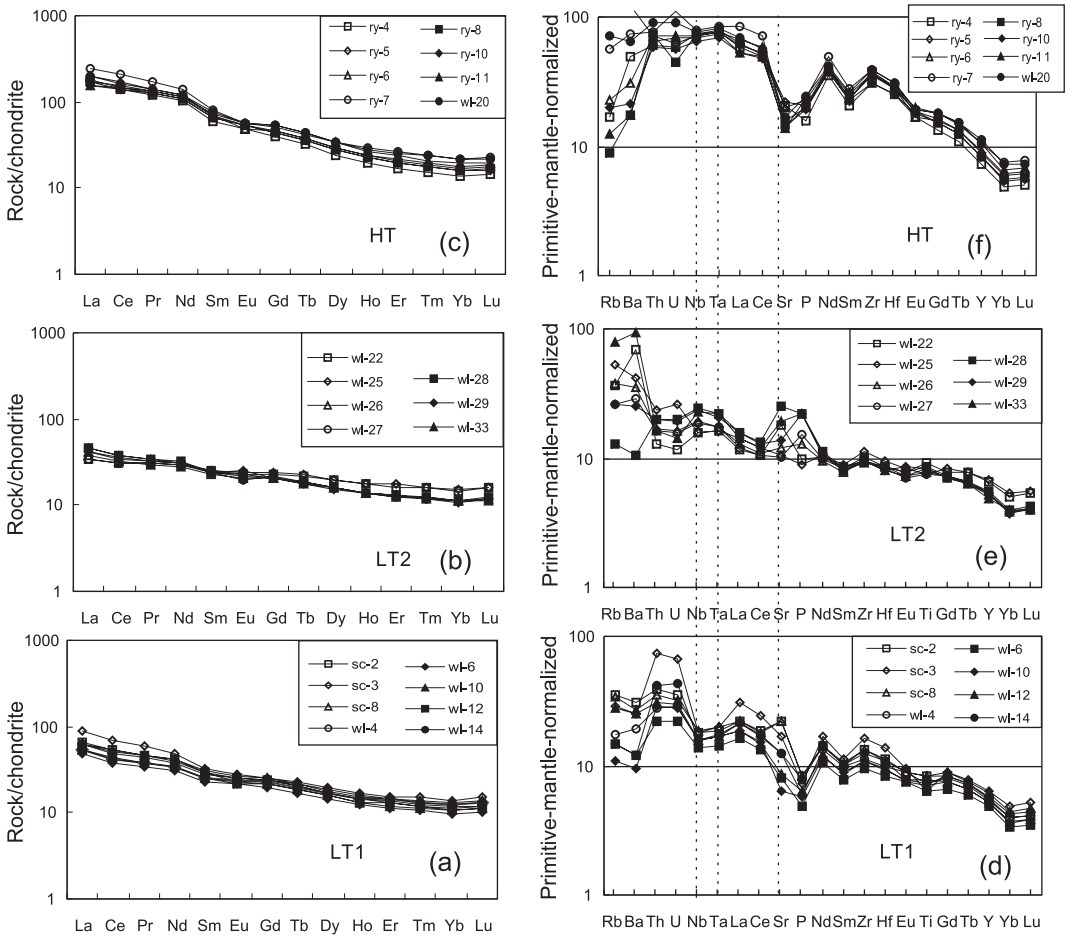

Fig. 6. REE pattern and trace element diagrams of the Emeishan basalts (normalized data from Sun and McDonough [51]). Sr and P negative anomalies reflect fractionations of plagioclase and apatite, respectively. Data not listed in Table 1 are after Xiao et al. [50].

array" and between the EMI and EMII mantle reservoirs. Generally, the HT basalts have higher $\varepsilon Nd(t)$ and lower $(^{87}Sr/^{86}Sr)_i$ values than the LT2 basalts, and the LT1 basalts have the lowest $\varepsilon Nd(t)$ values and highest $(^{87}Sr/^{86}Sr)_i$ ratios (Figs. 3, 4 and 7).

4.2.5. Oxygen isotope data

Oxygen isotope analysis was carried out for plagioclase and pyroxene phenocrysts in the Emeishan lavas (Table 3). Plagioclase and pyroxene were separated from LT1, LT2 and HT basalts. Several observations can be made from our data: (1) for both of LT and HT basalts, values of $\delta^{18}O$ for plagioclase are much higher than for pyroxene; (2) values of $\delta^{18}O$ for plagioclase range from 8.73‰ to 14.84‰ and are much higher than unaltered OIB whole rock and glass (4.6 to 7.50 [52]) and MORB (5.2 to 6.10 [53]); and (3) values of $\delta^{18}O$ for pyroxene ranging from 6.20‰ to 7.86‰ generally overlap the values of OIB.

5. Petrogenesis

The petrological and chemical variations of the Emeishan flood basalts from Binchuan are essentially controlled by a number of factors that include mantle temperature, lithosphere thickness, source composition and shallow level processes, such as crustal con-

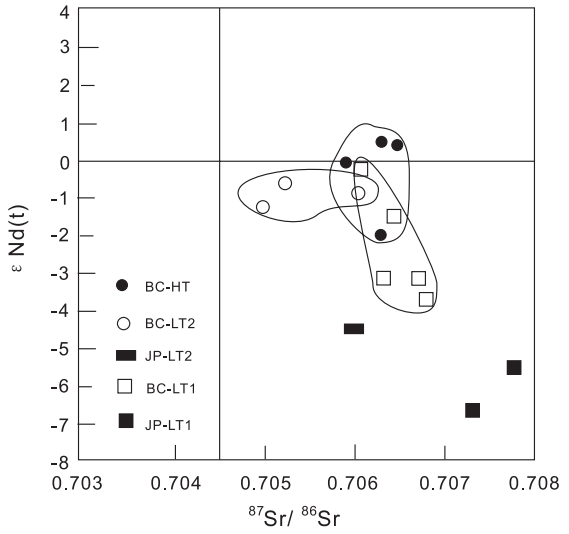

Fig. 7. $\varepsilon Nd(t)$ vs. $(^{87}Sr/^{86}Sr)_i$ isotope correlation diagram for the Emeishan flood basalts.

tamination and crystal fractionation, as is in fact recorded for other CFBs (e.g. [3,15,21,54,55]). The recognized systematic chemical variations of the LT1, LT2 and the HT basalts provide us with new evidence to identify their source composition and the temporal and genetic relationships among the LT1, LT2 and the HT types. In addition, these data enable us to assess the interaction of the Emeishan mantle plume with the lithosphere.

5.1. Magma fractionation

The distinct petrographical, chemical and isotopic features of the LT1, LT2 and the HT basalts reveal that they have experienced different crystal fractionation processes from parental magmas. Their low MgO contents (mostly <7 wt.%), Mg# (31–67) and Ni contents (<200 ppm for LT1 and <100 ppm for the LT2 and HT basalts; Table 1) suggest that they are not primary mantle melts and are far from the expected composition of melts in equilibrium with mantle peridotites.

The LT1 basalts may have undergone fractionation of clinopyroxene (cpx) and olivine (ol) from their parental magmas. This is supported by the presence of clinopyroxene and olivine (±plagioclase) as the dominant phenocrysts in these rocks, and is consistent with the positive correlations between Ni and Mg# (Fig. 5), SiO_2 and Th, and negative correlations between SiO_2 and Ni. Plagioclase fractionation may also be present, given the negative Sr and Eu anomalies and the presence of plagioclase phenocrysts in some rocks. Nevertheless, the lack of Sr anomalies in the majority of samples suggests that fractionation of plagioclase was not significant. The positive Sr negative anomalies are mainly associated with the samples (e.g. SC-2 and SC-8) which contain coarse bunches of plagioclase crystals (glomeroporphyritic textural types). This points to the effects of plagioclase accumulation. In summary, the petrographic and chemical data indicate dominant clinopyroxene and olivine fractionation and small plagioclase fractionation for the LT1 basalts. Similarly, clinopyroxene+olivine±plagioclase fractionation processes may also be applied to the LT2 basalts. The LT2 basalts include porphyritic basalts (WL-22~WL-29) at the top of unit 4 and interbedded aphyric and porphyritic basalts at the base of unit 4 and near the top of unit 3 (Fig. 2). The porphyritic basalts in the latter have phenocrysts of plagioclase, olivine and clinopyroxene, whereas the aphyric basalts have olivine and clinopyroxene microphenocrysts. The porphyritic basalts in the upper part of unit 4 exhibit relatively more extensive plagioclase fractionation than those in the lower part in unit 3 (Fig. 2). These features are consistent with the weak positive Sr anomalies of the porphyritic basalts at the

Table 3
Oxygen isotope composition of phenocryst minerals from Emeishan basalts

Rock type	Sample no.	Mineral	$\delta^{18}O$ (‰)
HT	RY-5	Plagioclase	14.84
	RY-8	Plagioclase	12.94
LT2	WL-23	Pyroxene	7.05
		Plagioclase	12.99
	WL-28	Pyroxene	6.20
		Plagioclase	10.80
	WL-31	Pyroxene	7.86
		Plagioclase	11.45
LT1	SC-6	Pyroxene	6.37
		Plagioclase	11.90
	SC-7	Pyroxene	6.97
		Plagioclase	8.73
	WL-6	Pyroxene	6.30
		Plagioclase	10.77
	UWG-2	Garnet	5.8±0.1
	SCO-1	Olivine	5.2±0.1

top of unit 4, and the weak negative Sr anomalies of the lavas in the stratigraphically lower sections (unit 3; Figs. 2 and 6). The HT basalts display significant negative Sr anomalies (Fig. 6), and a negative correlation between Mg# and Sr. This indicates extensive fractionation of plagioclase in the HT basalt, consistent with the presence of a larger proportion of plagioclase phenocrysts and less olivine phenocrysts than in the LT basalts. The lack of negative Eu anomalies in these evolved lavas probably reflects a high Eu^{3+}/Eu^{2+}ratio in the magmas [56].

We conclude that there are two differentiation trends for the Emeishan basalts from the Binchuan area. One is characterized by olivine and clinopyroxene fractionation in the LT basalts and the other by clinopyroxene+plagioclase±olivine fractionation in the HT basalts. This is also supported by inference of chemical composition from the 2(Fe+Mg)/P vs. Si/P diagram proposed by Ernst et al. [57]. A plot of these parameters (not shown in this paper, but available on request from the senior author) supports the clinopyroxene fractionation of the LT basalts and the fractionation of plagioclase and clinopyroxene for the HT basalts.

5.2. Crustal contamination

The recognition of crustally contaminated melts typically relies on identification of correlations between indices of fractionation and chemical and/or isotopic data. Correlations between MgO (negative) and SiO_2 (positive) contents with $(^{87}Sr/^{86}Sr)_i$ ratios are taken as evidence of progressive contamination of magmas while fractionation was taking place in litho-

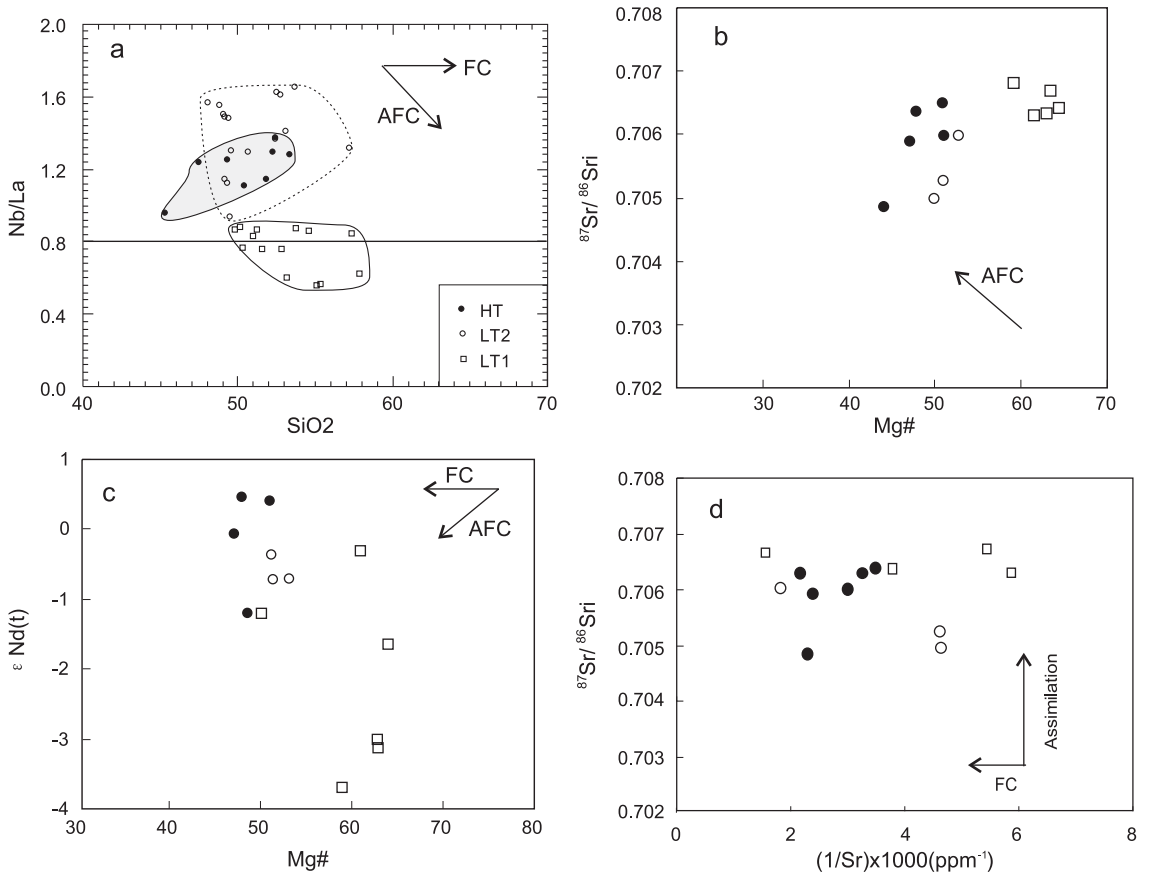

Fig. 8. SiO_2 vs. Nb/La, Mg# vs. $(^{87}Sr/^{86}Sr)_i$ and Nd(t), and 1/Sr vs. $(^{87}Sr/^{86}Sr)_i$ plots for the Emeishan basalts. Arrows indicate different magma variation trends. See text for explanation.

spheric magmas chambers. Xu et al. [3] proposed that the LT magmas (similar to LT1 group of this study) experienced two stages of contamination (the LT lavas assimilated crustal materials during ascent through conduits, and then have undergone an assimilation and fractional crystallization (AFC) style of contamination within a magma chamber prior to eruption. These processes can be attributed to contamination of the earlier melts, owing to disruption and magmatic erosion of the overlying lithospheric material by these melts, prior to the establishment of magma chambers. However, this interpretation might not be valid, because of a limited dataset (six samples). Xu et al. [3] also noticed the AFC trend is less evident for the LT samples. As shown in Fig. 5, Mg# and SiO_2 have no linear relationship between "crustal material" enriched LT and the OIB-like HT basalts. In addition, the SiO_2 vs. Nb/La plots (Fig. 8a) rule out significant AFC processes associated with petrogenesis. During magma evolution, AFC process should shows positive relationship between Mg# and Nd isotope, and negative relationship between Mg# and $(^{87}Sr/^{86}Sr)_i$ ratios. However, Fig. 8b,c shows reversed element and isotope relations. Moreover, $(^{87}Sr/^{86}Sr)_i$ vs. 1/Sr plots (Fig. 8d) show fractional crystallization dominated magma process, rather than AFC process.

The oxygen isotope study also provides an additional constraint on the genesis of the Emeishan basalts (Table 3). The well-defined and generally restricted oxygen isotope ratios of crustally uncontaminated oceanic basalts provide a powerful and unequivocal method to test the relative roles of crust and low mantle in the petrogenesis of CFBs [58]. Assimilation of crustal materials that have elevated $\delta^{18}O$ relative to the mantle-derived magmas should generate ^{18}O enrichment in the contaminated basalts with predictable correlated changes in radiogenic isotope ratios. Oxygen isotope data (Table 3, Fig. 9) suggest that pyroxenes have lower ^{18}O values (6.2‰ to 7.8‰), while plagioclase have extremely high $\delta^{18}O$ values (8.73‰ to 14.84‰). Because feldspar have very fast rates of O diffusion and thus are apt to reset its oxygen isotopes relative to pyroxenes [59], the extremely high $\delta^{18}O$ values for plagioclase may reflect higher extent of alteration and therefore cannot be used to represent their source $\delta^{18}O$ features. For this reason, only the $\delta^{18}O$ values for pyroxene phenocrysts are used for interpreting the petrogenesis of the basalts. The (^{18}O values for pyroxenes are still higher than that for the normal mantle (5.7±0.5‰ [60]), suggesting differential additions of crustal components in the processes of magma generation. It is possible that the crustal components may be derived from either enriched lithospheric mantle or plume head that trapped some crustal components (see Section 5.3.3 for further discussion).

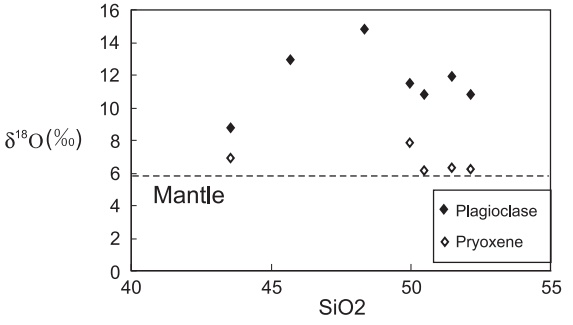

Fig. 9. ^{18}O vs. SiO_2 plots. Plotted data are pyroxene and plagioclase phenocrysts from the Emeishan basalts.

5.3. Source characteristics

5.3.1. Major element constraints

As mentioned above, the Emeishan basalts (Mg#=31–67) from the Binchuan area exhibit the effects of crystal fractionation processes from their parental magmas. In order to evaluate these effects in terms of variations of their chemical composition, we apply the method proposed by Klein and Langmuir [61] to extrapolate the evolved composition back to 8 wt.% MgO using the best-fit linear regression.

The correction of major element compositions of the Binchuan basalts at a constant MgO of 8% has been carried out for the LT1, LT2 and HT basalts, respectively (Fig. 10). A regression line was calculated for all samples, but only those with >5% MgO were used. The LT2 and HT magmas have similar Mg#8 that is lower than that of the LT1 magmas (Fig. 10a). Fe8 abundance increases from the LT1, LT2 to HT rocks (Fig. 10b). The LT and HT basalts have similar Si8. Fe8 abundance in primitive melts is positively correlated with the pressure [62] and negatively correlated with crustal assimilation [19]. This may suggest that the LT1 magmas were generated from shallower level than

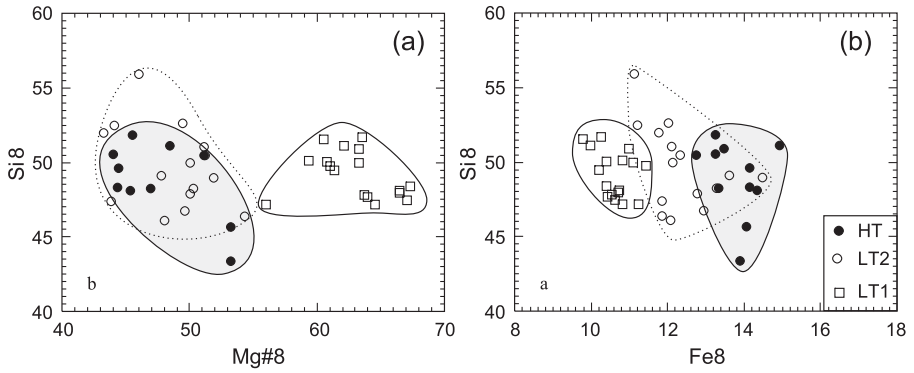

Fig. 10. Si8 vs. Mg#8 (a) and Si8 vs. Fe8 (b) plots for the Emeishan basalts.

the LT2 magmas. Another possibility is that they may have formed at the same level, but that the LT1 experienced more extensive crustal assimilation. However, this latter possibility can be ignored because the LT1 have higher Mg#8 than the LT2 magmas. Thus the variation of Fe8 abundance is a result of depth of generation. Alternatively, the relatively low Fe8 content may be due to their distinct mantle source, because refractory mantle source has a lower Fe8. The HT magmas with the highest Fe8 abundance suggest that these were produced from fertile mantle with an anomalously high potential temperature [3]. These differences between the LT and HT magmas strongly suggest that they originated from different mantle source areas.

5.3.2. Constraints from trace element compositions

Trace elements in basalts are efficient parameters for distinguishing their forming depths or the amount of extension and lithospheric thickness [59–63], and mantle property. The Ce/Yb ratios between the LT (Ce/Yb=14–18 (LT1) and 7–12.5 (LT2)) and HT (Ce/Yb=27–37) magmas suggest that the LT magmas may have been produced from a relatively shallow level. In contrast, the depth of melting from which the HT magmas formed is within lower mantle than that for LT magmas. This interpretation is also supported by Sm/Yb vs. La/Sm plots (Fig. 11). LT1 and LT2 lavas have similar low La/Sm and Sm/Yb ratios, and suggest high degree of partial melting from relatively shallow mantle. The La/Sm and Sm/Yb values for the HT basalts are extremely high, similar to Reunion [64], suggesting they were generated through smaller degrees of melting of a deeper mantle source. In primitive mantle normalized trace element patterns (Fig. 6), the LT1 lava displays remarkable negative anomalous of Nb and Ta, similar to arc basalts (see Fig. 12). In contrast, the HT lava is comparable with OIB and suggests plume origin.

5.3.3. Constraints from isotopic data

The $(^{87}Sr/^{86}Sr)_i$ and $\varepsilon Nd(t)$ isotopic values decrease and increase, respectively, with stratigraphic

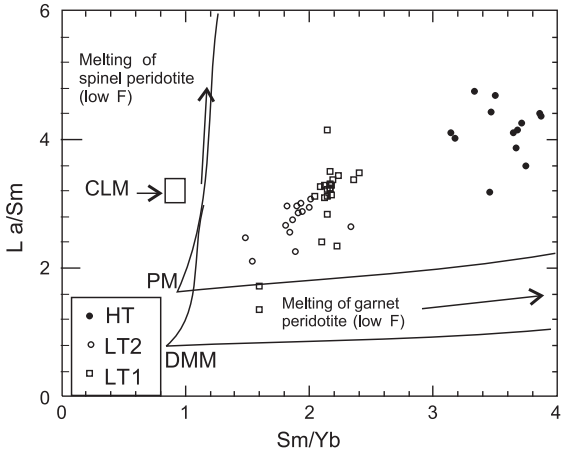

Fig. 11. La/Sm and Sm/Yb values for ECFB and other CFBs. Batch melting trends for garnet and spinel peridotite are after Lassiter and DePaolo [64]. Arrows denote the effect of decreasing melt fraction (F). Median composition of CLM is from McDonough [65]. This plot shows that LT1 and LT2 basalts have similar sources and underwent higher degree partial melting than that of HT lavas. Extremely high La/Sm and Sm/Yb ratios of HT basalts suggest that the HT lavas originated from garnet-bearing mantle source, comparable with Reunion [64], and experienced lower degree partial melting than LT1 and LT2 lavas.

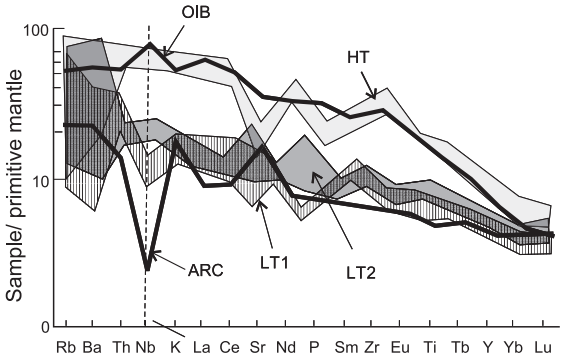

Fig. 12. Trace element patterns of Emeishan flood basalts normalized to primitive mantle of McDonough [65]. LT1 basalts show significant Nb and Ta negative anomalies that resembles arc basalts. LT2 group shows similar pattern to arc basalt but have positive Nb and Ta anomalies suggesting input of OIB melts. HT group show contrast pattern to LT1 and LT2 groups, and remarkably similar to OIB. Standard oceanic island basalt (OIB) after Sun and McDnough [51]; standard arc (ARC) sample after Hickey et al. [66].

height (Fig. 3e). The lower part and early stage of LT1 magmas exhibit the lowest $\varepsilon Nd(t)$ values ($\varepsilon Nd(t)=-3.76$) and highest $(^{87}Sr/^{86}Sr)_i$ ratios, in contrast the HT lavas (late stage) at the top of the succession have lowest $(^{87}Sr/^{86}Sr)_i$ ratios and highest $\varepsilon Nd(t)$ values ($\varepsilon Nd(t)=0.43$). These variation trends are consistent with the geochemical data. Both suggest that crustal signatures are becoming less significant from early stage LT1 to late stage HT magmas. We argue these crustal signatures are records of different mantle sources rather than crustal assimilation, due to elemental geochemistry, which ruled out significant crustal contamination during magma ascending (Section 5.2). In this aspect, isotope and fractionation indices plots provide consistent conclusion (Fig. 8). It means that LT magma generated from an enriched SCLM, whereas HT lava originated from fertile mantle source.

The oxygen isotope data for pyroxene suggest the crustal addition in the primary melts. It implies that the mantle source for the LT Emeishan basalts was fertile. There are two candidates, one is arc-like enriched SCLM and another is plume head that entrapped significant recycled crust components. However, the latter can be ruled out because arc-like LT basalt occurs strictly along the western margin of Yangtze plate, rather than distributed symmetrically on the top of plume (Fig. 1, see Sections 6 and 7 for further discussion). Spatial and temporal rock type variation can be successfully explained by this mantle-controlled model (see next section).

6. Mantle plume and lithosphere signatures

The distinct variations in the geochemical character of the LT and HT basalts may result from one of two reasons. They were either generated from different source areas, or produced from the same source, but through different evolutionary processes. We suggest that they were generated from different sources and our argument is based on the following points. First, the TiO_2 contents of the HT and the LT basalts display a significant gap, but have similar Mg# (Fig. 5). Second, they have distinct trace element characteristics, especially for high field strength elements (HFSE) (Fig. 6). Furthermore, a progressive chemical evolutionary trends (e.g. TiO_2 vs. Mg#) from LT1 to LT2, indicates that they also could have originated from a similar source area, but through different evolutionary processes.

A comparison of primitive mantle-normalized trace element patterns of HT, LT2 and LT1 rocks (Fig. 12) with OIB and arc basalts, suggest that they show distinguishable plume or lithospheric features. Fig. 12 shows that the LT1 magmas are similar to arc-related

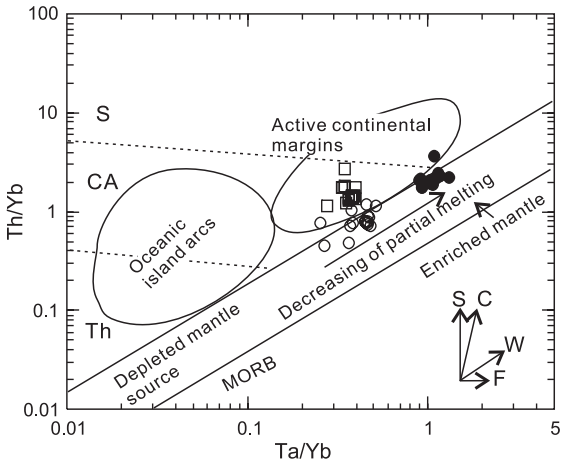

Fig. 13. Plots of Th/Yb vs. Ta/Yb for the Emeishan basalts from Binchuan area. Vectors indicate the influence of subduction components (S), within-plate enrichment (W), crustal contamination (C), and fractional crystallization (F). Dashed lines separate the boundaries of the tholeiitic (TH), calc-alkaline (CA), and shoshonitic (S) fields.

basalts [18]. We argue this type of magma was generated from enriched SCLM. The LT2 rocks also generally overlap the arc-type basalts, however, Nb and Ta positive anomalies can be recognized from the LT2 basalts. These features suggest the involvement of OIB melts. The HT rocks are similar to OIB and distinct from MORB. The HT magmas are relatively higher in large ion lithophile elements (LILE) and HFSE than the LT2. The Th/Yb vs. Ta/Yb plot (Fig. 13) indicates that the HT magmas are closer to an enriched mantle source and have less crustal signatures than the LT1 and LT2 magmas.

As discussed above, mantle plume signatures are shown in HT basalts that display strong enrichment in LILE and HFSE, and show OIB-like trace element patterns (Figs. 6 and 12). The ECFB is similar to other CFBs (e.g. Ethiopian [67]; northern Karoo [54]; Columbia River [68]) and consistent with plume-derived flood basalts as defined by Puffer [18]. Thus, we conclude that the HT lavas have a mantle plume origin.

7. Discussion

Our geochemical and isotopic data support that the LT lavas of the ECFB was generated from high degree of partial melting of SCLM, caused by heating from the impingement of a mantle plume. The western Yangtze craton was an active continental margin during the late Proterozoic [26–29]. The SCLM or mantle wedge at the western margin of the Yangtze craton may have been modified and enriched by subducted slab derived fluids [69,70] (also see Fig. 7 in [4]). When the Emeishan mantle plume impinged onto the western Yangtze craton, the enriched SCLM acted as an arc-type source to produce the arc-like LT [18]. In addition, Sr and Nd isotope composition from lavas in the Jinping area ($\varepsilon Nd(t)$=−4.49~−6.74; $(^{87}Sr/^{86}Sr)_i$=0.7059–0.7078; [50], which were initially located west of Binchuan [4], show more "crustal signatures" than those from Binchuan ($\varepsilon Nd(t)$=−0.34~−3.76; $(^{87}Sr/^{86}Sr)_i$=0.7049–0.7067). This suggests that the SCLM was increasingly enriched towards the western margin of the craton. Similar events characterize the Siberian Traps [16], the Karoo in South Africa [47], and the Central Atlantic Magmatic Province [72].

The western margin (present-day coordinates) of the Yangtze craton was a passive continental margin during Permian and middle Triassic times. Significant extension had affected the lithosphere of this passive margin, resulting in the formation of the Ganze-Litang rift, which opened to form a narrow ocean [4,24,35] (see also Fig. 1) in the late Permian. However, the upwelling of the Emeishan plume did not produce significant extension in the rest of the craton [23]. It is worth pointing out that the LT lavas, recognized so far, are distributed along the western margin of the Yangtze craton [3–5], see Fig. 1, whereas the HT lavas cover the whole area of ELIP. This spatial distribution of LT lavas is consistent with the postulated pre-existing enriched SCLM.

A high potential temperature of the mantle can be deduced from the presence of picrites [3,34]. Xu et al. [3] calculated a mantle potential temperature of about 1500~>1550 °C, which is much higher than normal mantle temperature (1280 °C). This high temperature along with the chemically enriched SCLM is the dominant factors that contributed to the formation of the LT lavas that show high degree partial melting.

The distinct origin of the Emeishan rock types and their temporal and spatial variations provide the basis for discussing the interaction process between the Emeishan mantle plume and the continental lithosphere. Here we propose a combined plume–SCLM interaction model to address the temporal and spatial variations of three types of lavas (LT1, LT2 and HT). These three rock types correspond to three stages of partial melting events, as explained below.

An early stage partial melting of previously enriched SCLM generated the LT1 lavas. The mantle plume had a passive role, in that it supplied heat. This plume-supplied heat caused a high degree of partial melting of the enriched SCLM, similar to the Parana-Etendeka [71]. There was little plume-derived melts that could have contributed to the source area of LT1 magmas. Therefore, the exposure area of LT1 lavas spatially corresponds to subduction-enriched SCLM, which parallels the western margin of the Yangtze craton.

Along with partial melting of the enriched SCLM, the mantle plume itself began to melt

producing OIB-like magmas. These plume melts penetrated into the overlying SCLM and/or LT1 magma, resulting in the formation of the LT2 lavas, which show some OIB features, such as positive anomalies of Nb and Ta, high Nb/La and Sm/Yb ratios. SCLM melting was then terminated, when it became depleted and refractory, because the plume-supplied heat was unable to cause further melting after extraction of the LT melts. Finally, a low degree partial melting of deep mantle (>75 km [64]) material generated HT magmas from the plume head. This type of magma displays close affinities with OIB and undoubtedly suggests a plume origin. The Nb/La vs. SiO_2 plot, along with combined isotope and fraction index plots (Fig. 8) do not show any correlation, suggesting that no significant AFC process had occurred, although there was some crustal contamination [3].

8. Conclusions

The Emeishan basaltic lavas at Binchuan include three types, LT1, LT2 and HT. The LT and HT basalts occur in the lower and upper successions, respectively.

Compared to OIB, the LT1 basalts are depleted in Nb, Ta and Rb, and have lower Nb/Th and Nb/La ratios suggesting a strong lithospheric signature. They are interpreted to have derived from a previously enriched SCLM and experienced olivine and clinopryoxene dominated fractional crystallization. Although geochemically similar to the LT1, LT2 have positive Nb and Ta anomalies and was generated from a source region similar to that of LT1, but with significant plume-derived melt contributions. Their parent magma experienced clinopyroxene and plagioclase fractionation.

On the other hand, the HT basalts are geochemically similar to OIB and may have been generated from mantle plume. Prior to the eruption, the HT magma has undergone plagioclase and clinopyroxene fraction with little crustal contamination.

Extensive interaction between the Emeishan plume and SCLM is considered important for the generation of the early stage of LT basalts. The spatial distribution of these basalt types and their geochemical and isotopic compositional variations, including the compositional variations, including the basalts in the Jinping area [4], suggest that there was an increasingly westward-enriched SCLM at the western Yangtze craton margin. This modified SCLM was the source of LT magmas. In contrast, HT magma was directly generated from the head of the Emeishan mantle plume, by large scale and low degrees of partial melting.

Acknowledgements

We thank Martin A. Menzies for constructive reviews. This study benefited from financial supports by the National Science Foundation of China (40234046 and 40272040). Field work was guided by Mr. Sha Shaoli. FP publishes with the permission of the Director of the Geological Survey of Western Australia.

References

[1] J.J. Mahoney, M.F. Coffin (Eds.), Large Igneous Provinces: Continental, Oceanic and Planetary Flood Volcanism, AGU Geophys. Monogr. 100 (1997) 438 pp.
[2] S.L. Chung, B.M. Jahn, Plume–lithosphere interaction in generation of the Emeishan flood basalts at the Permian–Triassic boundary, Geology 23 (1995) 889–892.
[3] Y.G. Xu, S.L. Chung, B.M. Jahn, G.Y. Wu, Petrologic and geochemical constraints on the petrogenesis of Permian–Triassic Emeishan flood basalts in southwestern China, Lithos 58 (2001) 145–168.
[4] L. Xiao, Y.G. Xu, S.L. Chung, B. He, H.J. Mei, Chemostratigraphic correlation of upper Permian lavas, from Yunnan Province, China: extent of the Emeishan large igneous province, Int. Geol. Rev. 45 (2003) 754–766.
[5] K.N. Huang, R.Y. Yang, X.C. Wang, A preliminary study on trace element geochemistry of Emeishan basalts from SW China, Acta Geol. Sin. 4 (1988) 49–60.
[6] X.Y. Song, M.F. Zhou, Z.Q. Hou, Z.M. Cao, Y.L. Wang, Y.G. Li, Geochemical constraints on the mantle source of the upper Permian Emeishan continental flood basalts, southwestern China, Int. Geol. Rev. 43 (2001) 213–225.
[7] J.J. Mahoney, Deccan Traps, in: J.D. Macdougall (Ed.), Continental Flood Basalts, Kluwer, Dordrecht, 1988, pp. 151–194.
[8] J.J. Mahoney, C. Nicollet, C. Dupuy, Madagascar basalts: tracking oceanic and continental sources, Earth Planet. Sci. Lett. 18 (1991) 350–363.
[9] C.J. Hawkesworth, M.S.M. Mantovani, D.W. Peate, Lithosphere remobilization during Parana magmatism, in: K.G. Cox, M. Menzies (Eds.), Oceanic and Continental Litho-

sphere: Similarities and Differences, J. Petrol. Spec. Issue, 1988, pp. 205–223.
[10] J.M. Hergt, D.W. Peate, C.J. Hawkesworth, The petrogenesis of Mesozoic Gondwana low-Ti flood basalts, Earth Planet. Sci. Lett. 105 (1991) 134–148.
[11] K. Gallagher, C.J. Hawkesworth, Dehydration melting and the generation of continental flood basalts, Nature (London) 358 (1992) 57–59.
[12] D.W. Peate, C.J. Hawkesworth, Lithospheric to asthenospheric transition in low-Ti flood basalts from southern Parana, Brazil, Chem. Geol. 127 (1996) 1–24.
[13] M.A. Richards, R.A. Duncan, V.E. Courtillot, Flood basalts and hot-spot tracks: plume heads and tails, Science 246 (1989) 103–107.
[14] R.S. White, D.P. McKenzie, Magmatism at rift zones: the generation of volcanic continental margins and flood basalts, J. Geophys. Res. 94 (1989) 7685–7730.
[15] N.T. Arndt, U. Christensen, The role of lithospheric mantle in continental flood volcanism: thermal and geochemical constraints, J. Geophys. Res. 97 (1992) 10967–10981.
[16] P.C. Lightfoot, A.J. Naldrett, N.S. Gorbachev, W. Doherty, V.A. Fedorenko, Geochemistry of the Siberian trap of the Noril'sk area, USSR. With implication for the relative contributions of crust and mantle to flood basalt magmatism, Contrib. Mineral. Petrol. 104 (1990) 631–644.
[17] R. Kerrich, D. Wyman, J. Fan, W. Bleeker, Boninite series: low Ti–tholeiite associations from the 2.7 Ga Abitibi greenstone belt, Earth Planet. Sci. Lett. 164 (1998) 303–316.
[18] J.H. Puffer, Contrasting high field strength element contents of continental flood basalts from plume versus reactivated-arc sources, Geology 29 (2001) 675–678.
[19] Z.X. Peng, J. Mahoney, P. Hooper, C. Harris, J. Beane, A role for lower continental crust in flood basalt genesis? isotopic and incompatible element study of the lower six formations of the Western Decan Traps, Geochim. Cosmochim. Acta 58 (1994) 267–288.
[20] M.S. Fram, C.E. Lesher, Generation and polybaric differentiation of East Greenland early tertiary flood basalts, J. Petrol. 38 (1997) 231–275.
[21] D.P. McKenzie, M.J. Bickle, The volume and composition of melt generated by extension of the lithosphere, J. Petrol. 29 (1988) 625–679.
[22] M. Olafsson, D.H. Eggler, Phase relations of amphibole, amphibole-carbonate and phlogopite-carbonate peridotite: petrological constraints on the asthenosphere, Earth Planet. Sci. Lett. 64 (1983) 305–315.
[23] B. He, Y.G. Xu, S.L. Chung, L. Xiao, Y.M. Wang, Sedimentary evidence for a rapid, kilometer-scale crustal doming prior to the eruption of the Emeishan flood basalts, Earth Planet. Sci. Lett. 213 (2003) 391–405.
[24] X.X. Mo, F.X. Lu, S.Y. Shen, et al., Sanjiang Tethyan Volcanism and Related Mineralization, Geological Publishing House, Beijing, 1993, 267 pp.
[25] D.L. Zhong, The Paleo-Tethys Orogen in Western of Yunnan and Sichuan, Science Press, Beijing, 1998, 231 pp.
[26] B.L. Cong, Formation and Evolution of the Panxi Paleorift, Science Press, Beijing, 1988, pp. 217–250.
[27] M.K. Zhou, Y.R Liu, The Geological Characteristics and Tectonic Evolution in the Xichang–Midu–Yunnan Region, Chongqing Publishing House, Chongqing, China, 1988, 187 pp.
[28] C.M. Sun, V. Vuagnat, Proterozoic ophiolites from Yanbian and Shimian (Sichuan Province, China): Petrography, geochemistry, petrogenesis, and geotectonic environment, Schweiz. Mineral. Petrogr. Mitt. 72 (1992) 389–413.
[29] W.Z. Shen, S.J. Xu, The isotope-geochemistry characteristics of the Jinning Period granites on the margin of the Yangzte Plate, in: Y.F. Zheng (Ed.), Geochemical Dynamics, Science Publishing House, Beijing, 1999, pp. 258–270.
[30] M.F. Zhou, J. Malpas, X.Y. Song, P.T. Robinson, M. Sun, A temporal link between the Emeishan large igneous province (SW China) and the end-Guadalupian mass extinction, Earth Planet. Sci. Lett. 196 (2002) 113–122.
[31] L. Xiao, Y.G. Xu, J.F. Xu, B. He, F. Pirajno, Chemostratigraphy of flood basalts in the Ganze-Litang region and Zhongza Block: implication for a western extension of the Emeishan large igneous province, SW China, Acta Geol. Sin., J. Geol. Soc. China 78 (2004) 61–67.
[32] Y.X. Zhang, Y.N. Luo, Z.X. Yang, Panxi Rift, Geological Publishing House, Beijing, 1988, 466 pp.
[33] G.M. Thompson, J.R. Ali, X.Y. Song, Emeishan basalts, SW China: reappraisal of the formation's type area stratigraphy and a discussion of its significance as a large igneous province, J. Geol. Soc. (London) 158 (2001) 593–595.
[34] Z.C. Zhang, F.S. Wang, Picritic lavas discovered in the Emeishan large igneous province, Geol. Rev. 48 (2002) 448.
[35] S.L. Chung, B.M. Jahn, G.Y. Wu, The Emeishan flood basalt in SW China: a mantle plume initiation model and its connection with continental break-up and mass extinction at the PermianTriassic boundary, in: M. Flower, S.L. Chung, G.H. Lo (Eds.), Mantle Dynamics and Plate Interaction in East Asia, AGU Geodyn. Ser. 27 (1998) 47–58.
[36] F. Pirajno, Ore Deposits and Mantle Plumes, Kluwer Academic Publishers, Dordrecht, 2001, 509 pp.
[37] J.Y. Lin, Spatial distribution and geological characteristics of the Permian Emeishan basalts in SW China, Chin. Sci. Bull. 12 (1986) 929–932.
[38] Bureau of geology and mineral resources of Yunnan province, Regional geology of Yunnan province. Geological Publishing House, Beijing, 1990, 728 pp.
[39] Bureau of geology and mineral resources of Sichuan province, Regional geology of Sichuan province, Geological Publishing House, Beijing, 1990, 745 pp.
[40] Y. Liu, H.C. Liu, X.H. Li, Simultaneous and precise determination of 40 trace elements in rock samples using ICP-MS, Geochimica 25 (1996) 552–558.
[41] C.X. Mao, B.Q. Zhu, Z.E. Zhu Si, R.S. Huang, Measurement techniques and applications of the Sm–Nd isotopic system, Geochemica 1 (1989) 36–41.
[42] Y.G. Xu, Evidence for crustal components in the mantle and constraints on crustal recycling mechanisms: pyroxenite xenoliths from Hannuoba, North China, Chem. Geol. 182 (2002) 301–322.

[43] X.R. Liang, G.J. Wei, X.H. Li, Y. Liu, Precise measurement of 1433Nd/144Nd and Sm/Nd ratios using multiple-collectors inductively coupled plasma-mass spectrometer (MS-ICPMS), Geochemica 32 (2003) 91–96.
[44] Y.F Zheng, Z.R. Wang, S.G. Li, Z.F. Zhao, Oxygen isotope equilibrium between eclogite minerals and its constraints on mineral Sm–Nd chronometer, Geochim. Cosmochim. Acta 66 (2002) 625–634.
[45] D.A. Swanson, T.L. Wright, P.R. Hooper, R.D. Bentley, Revisions in stratigraphic nomenclature of the Columbia River basalt Group, U.S. Geol. Surv. Bull. 1457G (1979) G1–G59.
[46] K.G. Cox, C.J. Hawkesworth, Geochemical stratigraphy of the Deccan Traps at Mahabaleshwar, Western Ghats, India, with implications for open system magmatic processes, J. Petrol. 26 (1985) 355–377.
[47] T.B. Bowen, J.S. Marsh, M.P. Bowen, H.V. Eales, Volcanic rocks of the Witwatersrand triad, South Africa I: description, classification, and geochemical stratigraphy, Precambrian Res. 31 (1986) 297–324.
[48] J.S. Marsh, P.R. Hooper, J. Rehacek, A.R. Duncan, Stratigraphy and age of Karoo basalts of Lesotho and implications for correlations within the Karoo igneous province, in: J.J. Mahoney, M.F. Coffin (Eds.), Large Igneous Province: Continental, Oceanic, and Planetary Flood Volcanism, Am. Geophys. Union Geophys. Monogr. 100 (1997) 247–272.
[49] J.S. Marsh, A. Ewart, S.C. Milner, A.R. Duncan, R. McG. Miller, The Etendeka igneous province: magma types and their stratigraphic distribution with implications for the evolution of the Parana–Etendeka flood basalts province, Bull. Volcanol. 62 (2001) 464–486.
[50] L. Xiao, Y.G. Xu, B. He, Emeishan mantle plume–subcontinental lithosphere interaction: Sr–Nd and O isotopic evidences from low-Ti and high-Ti basalts, Geol. J. China Univ. 9 (2003) 207–217.
[51] S.S. Sun, W.F. McDonough, Chemical and isotopic systematics of oceanic basalts: implications for mantle composition and processes, in: A.D. Saunders, M.J. Norry (Eds.), Magmatism in Ocean Basins, Geol. Soc. London Spec. Publ. 42 (1989) 313–345.
[52] R.S. Harmon, J. Hoefs, Oxygen isotope heterogeneity of the mantle deduced from global 18O systematics of basalts from different geotectonic settings, Contrib. Mineral. Petrol. 120 (1995) 95–114.
[53] E. Ito, W.M. White, C. Gopel, The O, Sr, Nd and Pb isotope geochemistry of MORB, Chem. Geol. 62 (1987) 157–176.
[54] R.J. Sweeney, A.R. Duncan, A.J. Erlan, Geochemistry and petrogenesis of central Lebombo basalts of the Karoo igneous province, J. Petrol. 35 (1994) 95–125.
[55] S. Turner, C. Hawkesworth, The nature of the subcontinental mantle: constraints from the major-element composition of continental flood basalts, Chem. Geol. 120 (1995) 295–314.
[56] F.A. Frey, M.O. Garcia, W.S. Wise, A. Kennedy, P. Gurriet, F. Albarede, The evolution of Mauna Kea volcano, Hawaii: petrogenesis of tholeiitic and alkali basalts, J. Geophys. Res. 96 (1993) 14347–14375.
[57] R.E. Ernst, A.D. Fowler, T.H. Pearce, Modeling of igneous fraction and other processes using Pearce diagrams, Contrib. Mineral. Petrol. 100 (1988) 12–18.
[58] J.A. Baker, G.G. Macpherson, M.A. Menzies, M.F. Thirlwallet, M. Al-Kadasi, D.P. Mattey, Resolving crustal and mantle contributions to continental flood volcanism, Yemen; constraints from mineral oxygen isotope data, J. Geol. 41 (2000) 1806–1820.
[59] Y.F. Zheng, Z.F. Zhao, S.G. Li, B. Gong, Oxygen isotope equilibrium between ultrahigh-pressure metamorphic minerals and its constraints on Sm–Nd and Rb–Sr chronometer, in: D. Vance, W. Muller, I.M. Villa (Eds.), Geochronology: Liking the Isotopic Record with Petrology and Texture, Geol. Soc. London Spec. Publ. 220 (2003) 93–117.
[60] D. Mattey, D. Lowry, C. Macpherson, Oxygen isotope composition of mantle peridotite, Earth Planet. Sci. Lett. 128 (1994) 231–241.
[61] E.M. Klein, C.H. Langmuir, Global correlations of ocean ridge basalt chemistry with axial depth and crustal thickness, J. Geophys. Res. 92 (1987) 8089–8115.
[62] K. Hirose, I. Kushiro, Partial melting of dry peridotites at high pressure: determination of compositions of melts segregated from peridotite using aggregates of diamond, Earth Planet. Sci. Lett. 114 (1993) 477–489.
[63] D.P. McKenzie, R.K. O'Nions, Partial melt distribution from inversion of rare earth element concentrations, J. Petrol. 32 (1991) 1021–1091.
[64] J.C. Lassiter, D.J. DePaolo, Plume/lithosphere interaction in the generation of continental and oceanic flood basalts: chemical and isotopic constraints, in: J.J. Mahoney, M.F. Coffin (Eds.), Large Igneous Province: Continental, Oceanic, and Planetary Flood Volcanism, American Geophysical Union Geophysical Monography vol. 100 (1997) pp. 335–355.
[65] W.F. McDonough, Constraints on the composition of the continental lithospheric mantle, Earth Planet. Sci. Lett. 128 (1990) 231–241.
[66] R.L. Hickey, F.A. Frey, C. Gerlach, Multiple sources for basaltic arc rocks from the southern zone of the Andes: trace element and isotopic evidence for contributions from subducted oceanic crust, mantle, and continental crust, J. Geophys. Res. 91 (1986) 5963–5983.
[67] R. Pik, C. Deniel, C. Coulon, G. Yirgu, B. Marty, Isotopic and trace element signatures of Ethiopian flood basalts: evidence for plume–lithosphere interactions, Geochim. Cosmochim. Acta 63 (1999) 2263–2279.
[68] A. Keer, Lithosphere thinning during the evolution of continental large igneous provinces: a case study from North Atlantic Tertiary province, Geology 22 (1994) 1027–1039.
[69] P.R. Hooper, C.J. Hawkesworth, Isotopic and geochemical constraints on the origin and evolution of the Columbia River basalts, J. Petrol. 34 (1993) 1203–1246.
[70] A.E. Ringwood, Slab–mantle interactions, petrogenesis of intraplate magmas and structure of the upper mantle, Chem. Geol. 82 (1990) 187–207.

[71] S.P. Turner, C.J. Hawkesworth, K. Gallagher, K. Stewart, D.W. Peate, M.S.S. Mantovani, Mantle plumes, flood basalts and thermal models for melt generation beneath continents: assessment of a conductive heating model and application to the Parana, J. Geophys. Res. 101 (1996) 11503–11518.

[72] J.H. Puffer, Eastern North American flood basalts in the context of the incipient breakup of Pangea, in: J.H. Puffer, P.C. Ragland (Eds.), Eastern North American Mesozoic Magmatism, Special Paper-Geological Society of America, vol. 268, 1992, pp. 95–118.